CAMS Service Evolution

D5.4 Extended dry deposition scheme in LOTOS-EUROS

Due date of deliverable	30-6-2025
Submission date	30-6-2025
File Name	CAMAERA-D5.4-v1.1
Work Package /Task	WP5 T5.3
Organization Responsible of Deliverable	TNO
Author name(s)	H.J. Jonas, X. Ge, L. Geers, R. Kranenburg, C. Halevy
Revision number	1.1
Status	
Dissemination Level	PU

The CAMAERA project (grant agreement No 101134927) is funded by the European Union.
Views and opinions expressed are however those of the author(s) only and do not necessarily reflect those of the European Union or the Commission. Neither the European Union nor the granting authority can be held responsible for them.

1 Executive Summary

The Copernicus Atmosphere Monitoring Service (CAMS), part of the European Union's Copernicus Space Programme, provides high quality, near real-time atmospheric composition data for air quality, climate change and pollution mitigation by combining satellite observations with advanced numerical modelling. In close collaboration with other CAMS initiatives, the CAMAERA (CAMS AERosol Advancement) project aims to significantly enhance the aerosol modelling within CAMS by integrating new data sources, improving the representation of secondary aerosols and their precursors, and developing prototype service elements that go beyond the current state of the art.

This deliverable under Work Package 5 (WP5) specifically targets improvements in the modelling of aerosol emissions and dry deposition. The main objective was to extend the LOTOS-EUROS dry deposition scheme to better account for dynamic and diverse surface types. As planned in Task WP5.3, an updated scheme was implemented, including a three-tier approach, new deposition parameters, satellite-derived leaf area index and spatially and temporally explicit tree species and height as demonstrated in several case studies, which show improved modelling capabilities. The updates highlight the flexibility and extensibility, allowing users to test different land use maps and deposition parameters.

The updates affect aerosol simulations in two ways: indirectly, by influencing gas phase chemistry and subsequent aerosol formation; and directly, through changes in land surface characteristics, such as roughness length, which affect gas-phase and aerosol dry deposition rates. Future work will focus on comparing modelled and observed aerosol concentrations to identify and address shortcomings in aerosol deposition modelling, taking advantage of the adaptability of the three-tiered approach.

Table of Contents

2 Introduction

2.1 Project Background

The European Union's flagship space program, Copernicus, provides a key service to European society by transforming investments in space infrastructure into high quality information products. The Copernicus Atmosphere Monitoring Service (CAMS, https://atmosphere.copernicus.eu) uses the information content of Earth observation data to monitor the composition of the atmosphere. By combining satellite observations with numerical modelling using data assimilation and inversion techniques, CAMS provides a wealth of information in near-real time to answer questions related to air quality, climate change and air pollution and mitigation, energy, agriculture, etc. CAMS provides both global atmospheric composition products using ECMWF's Integrated Forecasting System (IFS) - hereafter referred to as the global production system - and European regional products provided by an ensemble of eleven regional models - the regional production system.

The CAMS AERosol Advancement (CAMAERA) project will provide major improvements in the aerosol modelling capabilities of the regional and global systems, in the assimilation of new data sources, and in the representation of secondary aerosols and their precursors. In this way, CAMAERA will improve the quality of the key products of the CAMS service, thereby helping CAMS to better respond to user needs such as air pollution monitoring and the achievement of sustainable development goals. To achieve this, CAMAERA will develop new prototype service elements of CAMS that go beyond the current state of the art. It will do this in very close collaboration with CAMS service providers and other Tier 3 projects. In particular, CAMAERA will complement the research topics addressed by CAMEO, which focuses on the processing of novel satellite data, the improvement of the data assimilation and inversion capabilities of the CAMS production system, and the provision of uncertainty information on CAMS products.

2.2 Scope of this deliverable

2.2.1 Objectives of this deliverable

WP5 focuses on the development, implementation and evaluation of new parameterizations for online aerosol or precursor gas emissions and dry deposition.

The LOTOS-EUROS dry deposition scheme will be extended to use inputs that better differentiate surface types and their temporal evolution.

2.2.2 Work performed in this deliverable

In this deliverable the work as planned in the Description of Action (DoA, WP 5, task 5.3) was carried out: Extension of the LOTOS-EUROS dry deposition scheme. The extension was demonstrated for a number of cases (see below).

2.2.3 Deviations and counter measures

No deviations have been made.

2.2.4 CAMAERA Project Partners:

HYGEOS	HYGEOS SARL
ECMWF	EUROPEAN CENTRE FOR MEDIUM-RANGE WEATHER FORECASTS
Met Norway	METEOROLOGISK INSTITUTT
RC.io	RESEARCHCONCEPTS IO
BSC	BARCELONA SUPERCOMPUTING CENTER-CENTRO NACIONAL DE SUPERCOMPUTACION
KNMI	KONINKLIJK NEDERLANDS METEOROLOGISCH INSTITUUT-KNMI
SMHI	SVERIGES METEOROLOGISKA OCH HYDROLOGISKA INSTITUT
FMI	ILMATIETEEN LAITOS
MF	METEO-FRANCE
TNO	NEDERLANDSE ORGANISATIE VOOR TOEGEPAST NATUURWETENSCHAPPELIJK ONDERZOEK TNO
INERIS	INSTITUT NATIONAL DE L ENVIRONNEMENT INDUSTRIEL ET DES RISQUES - INERIS
IOS-PIB	INSTYTUT OCHRONY SRODOWISKA - PANSTWOWY INSTYTUT BADAWCZY
FZJ	FORSCHUNGSZENTRUM JULICH GMBH
AU	AARHUS UNIVERSITET
ENEA	AGENZIA NAZIONALE PER LE NUOVE TECNOLOGIE, L'ENERGIA E LO SVILUPPO ECONOMICO SOSTENIBILE

2.3 Outline

First, an overview is given of the extension of the dry deposition scheme in LOTOS-EUROS. Chapter 3 explains a Three-Tiered Land Use Approach that enables fine-grained control over the deposition behavior per type of vegetation or underground. The benefits of this approach are demonstrated in the following chapters. Chapter 4 describes the update of the deposition parameters of the most prominent vegetation of arable and semi-natural land in North-West Europe and its effect on deposition fluxes. Chapter 5 is about changes to the Leaf Area Index of certain tree species based on satellite images and how this affects deposition of N-compounds. Finally, Chapter 6 demonstrates the effect of a further specification of tree species and changes in tree height for these species on the deposition of nitrogen compounds over Germany. Chapter 7 closes with some general conclusions.

3 Extension of LOTOS-EUROS dry deposition scheme

The extension described in this report involves a novel approach for the land use characterization that forms the basis for the parametrization of the dry gas and particle deposition scheme. Each grid cell in LOTOS-EUROS is characterized by fractions of several types of land use in that particular grid cell. The land use classes are used to establish deposition velocities and surface roughness. It is also required to determine biogenic emission fluxes, such as isoprene and terpene emissions from forests. Land use and land cover are also important for calculations of NO emissions from soil, wind-blown dust, and agricultural emissions from ploughing, etc.

The first investigations using this new approach were focused on a differentiation of tree species and height in European forests, a differentiation of vegetation in agricultural land, semi-natural areas and grass land, and an adaptation of the growing seasons for different crops. Those are presented in the next sections.

3.1 The Three-Tiered Land Use Approach

From LOTOS-EUROS v3.0.000, the land use classification is based on a three-tiered land use approach: climate zone, land use, and vegetation types as Tier 1, Tier 2 and Tier 3, respectively. In this way, a coniferous tree in Norway can be distinguished from a coniferous tree in the Netherlands by their climate zones (continental and temperate, respectively), and it is possible to define model parameters specific to vegetation types. For example, the deposition characteristics on potato plants may be very different from those on maize, despite the fact that they share the same land use class (arable land). Figure 1 schematically shows how the three tiers are overlayed on top of each other and that multiple maps can be used to construct a three-tiered map.

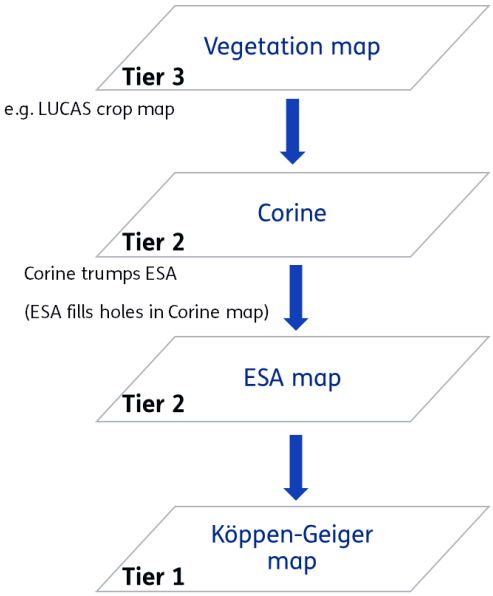

Figure 1: Schematic overview of the 3-tiered LU approach.

The Tier 1 information is based on the Köppen-Geiger climate zone map with a 1/6° × 1/12° resolution and a classification of 31 climate zones (Beck et al., 2018). For LOTOS-EUROS, the original map is regridded to a 1/10° × 1/12° resolution and the climate zones were recombined into six global climate zones, based on precipitation and temperature data. In

addition, a seventh class was added to cover the oceans. Figure 2 shows the climate zone classification used in LOTOS-EUROS v3.0.

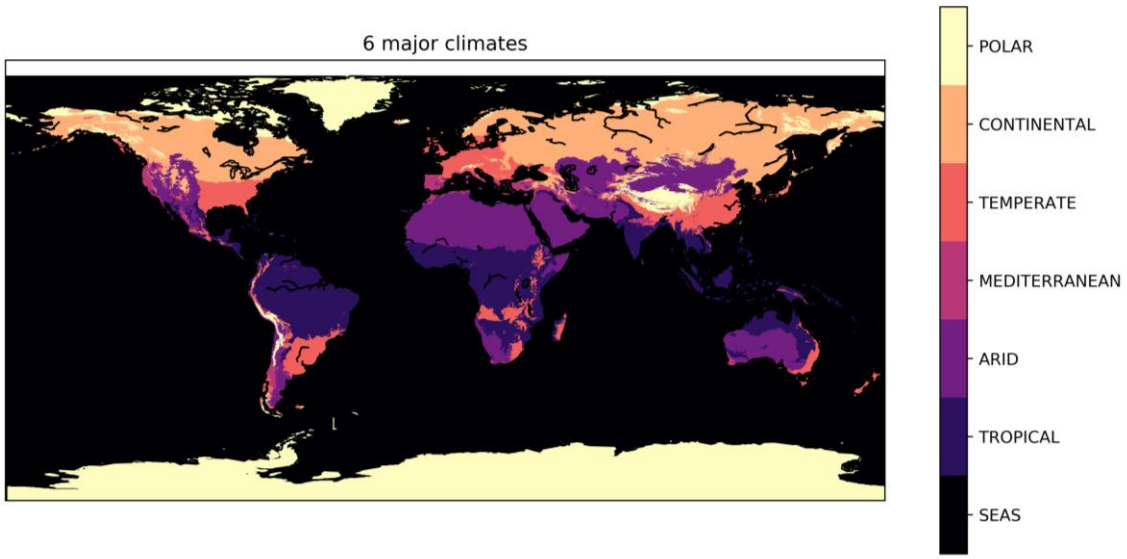

Figure 2: Tier 1, the climate zone classification.

Tier 2 consists of land-use information. Currently, the ESA2015 (Land Cover 2015 (raster 100 m), global, yearly – version 3 — Copernicus Land Monitoring Service, 2025) and CORINE2018 (CORINE Land Cover 2018 (raster 100 m), Europe, 6-yearly - version 2020_20u1, May 2020, 2025) maps are combined into one map. ESA2015 is a global land cover map based on satellite data with a spatial resolution of 300m. Corine2018 is a pan-European land cover inventory covering 44 classes with a spatial resolution of 100m, which makes it more detailed than the ESA map. After converting both the Corine and the ESA maps to the required resolution and domain, they are combined. Corine provides a more detailed specification of land cover, but it does not provide data for the complete map (i.e., no data in seas). Therefore, the data from the Corine map is leading, but in places where no data is available, the ESA map is used to fill in the gaps.

Tier 3 represents the vegetation types for each land use class. Since the amount of vegetation types differs per land use class, Tier 2 and 3 names are combined in the deposition parameter table. Thus, every land use dependent deposition model parameter has dimensions climate zone and land use/vegetation type. As an optional step, local, national or regional crop maps may be used to further specify the vegetation types, for instance, using data from the Land Use and Coverage Area frame Survey (Joint Research Centre Data Catalogue - LUCAS Copernicus 2018 - European Commission, 2025) .

Using this new classification means that the dry-deposition-related parameters need to be defined for each climate zone/vegetation combination present in the three-tiered land use map. For that reason, they are no longer hard-coded in the model. Hence, two NetCDF input files need to be provided to LOTOS-EUROS, namely, a fraction map of the land use classes constructed as shown above, and a table of deposition parameters for each land use class. Within the model, it is checked that all classifications in the map are present in the parameter file as well. The combination of the map and the parameter file allows users to change and extend the deposition properties and land-use classification without modifying the model code. Now, with the Three-Tiered Land Use Approach, the user is free to adjust and compose their own maps and classifications with the corresponding deposition parameters.

Further details on the implementation and the use of this approach in LOTOS-EUROS can be found in the LOTOS-EUROS Users' Guide (Segers et al., 2025) and the Reference Guide (Manders et al., 2025), both to be published online in the next month.

3.2 DEPAC model – a short description

LOTOS-EUROS implements the DEPAC model for the calculation of dry gas deposition fluxes (van Zanten et al., 2010). For background knowledge, a short description is provided here. It uses the well-known resistances approach to calculate the deposition of acidifying compounds (originally) and is developed by the Dutch National Institute for Public Health and the Environment (RIVM) with extensions and necessary adaptations by TNO for application in LOTOS-EUROS. It is primarily used to estimate the deposition fluxes of species such as NH_x, NO_x, and SO_x onto different surfaces.

The model is structured around the resistance approach, where the deposition flux is calculated via:

$$F = -V_d \, \Delta\chi \qquad \textbf{Equation 3.1}$$

where F is the (deposition) flux, V_d is the deposition velocity and $\Delta\chi$ is the concentration difference between the atmosphere and the surface.

Via the resistances F_1, F_2, F_3, and F_4, as schematically depicted in Figure 3, the deposition velocity is defined as:

$$V_d = \frac{1}{R_a} + \frac{1}{R_b} + \frac{1}{R_c} \qquad \textbf{Equation 3.2}$$

where R_a is aerodynamic resistance, R_b is the quasi-laminar layer resistance, and R_c the canopy resistance defined as:

$$R_c = \left(\frac{1}{R_w} + \frac{1}{R_s} + \frac{1}{R_{soil,eff}} \right)^{-1} \qquad \textbf{Equation 3.3}$$

where R_w is the external leaf surface resistance, R_s the stomatal resistance, and $R_{soil,eff}$ is the effective soil resistance. The Three-Tiered Land use Approach now enables us to set the values of parameters for these three resistances per vegetation type & climate zone. Further details are provided in (van Zanten et al., 2010).

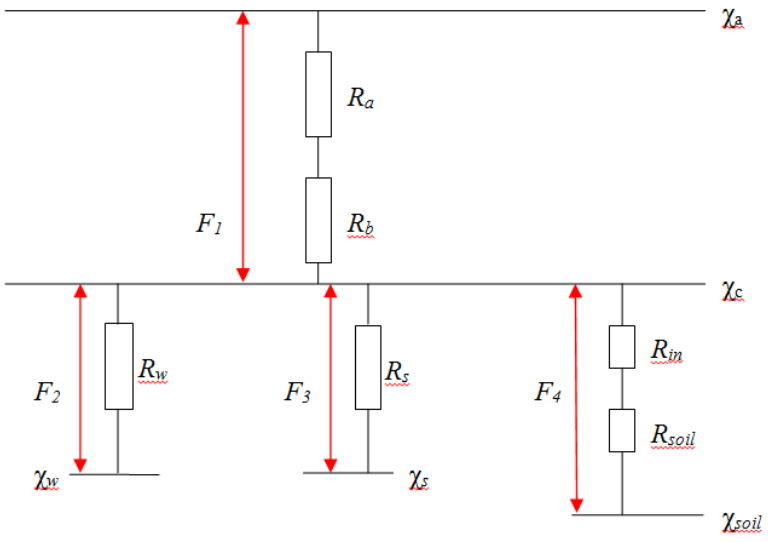

Figure 3 The resistance approach of DEPAC (van Zanten et al., 2010).

3.3 Dry deposition parameters

Parameter values for the dry gas deposition model DEPAC and the dry aerosol deposition model (Zhang et al., 2001) need to be supplied per climate zone and per land use / vegetation type. For each land use class, there needs to be at least a default vegetation type. This ensures that calculations can still be performed in case the land use fraction map is only specified to Tier 2 (i.e. no differentiation in vegetation type).

The parameters in the deposition parameter data file have default values originating from the DEPAC model, with a few small changes. The most important is the parametrizations for Mediterranean vegetation. These were collected from the DO_3SE model (Mills et al., 2010). Specifically, the Jarvis parameters for stomatal resistance were adapted for the Mediterranean climate zone for arable land, permanent crops, and forest classes.

4 Detailing the vegetation dry deposition parameters

4.1 Introduction

Gaseous species in the air have various ways to dry deposit: through the soil, and the stomata and the external leaf surfaces of plants. How fast a plant can take up pollutants is specific to each vegetation type as they have adapted themselves to their environment by evolution e.g. depending on the weather, and availability of water and nutrients.

As introduced in the previous Section 3.1, LOTOS-EUROS v3.0 now uses a three-tiered land use approach based on the three tiers: climate zone, land use class and vegetation type to easily distinguish deposition parameters of, for example, a coniferous tree in Norway from one in France by their different climate zone. This new method allows for detailing dry deposition parameters specific for local vegetation types adapted for their local climate. Moreover, it makes it possible to differentiate between different vegetation types, e.g. crops, trees, or bushes, with different characteristics that were previously grouped in a single broad land use category. The aim of this work is to improve the description of the dry deposition via the stomata and external leaf surfaces of plants in Northwest Europe by detailing the deposition parameters of the vegetation on arable land and semi-natural land in the temperate climate.

The vegetations that were selected in this work are either the most abundant vegetation type, or their growing season was retrieved from the German meteorological service DWD (DWD Climate Data Center, 2024). In principle, on arable land, wheat is the most abundant vegetation. However, as the default parameters for arable land are based on the properties of wheat, its parameters are not updated in this work. Figure 4 shows the land use fraction map of the listed land use classes in Table 1. The nomenclature of the three-tiered approach follows three letter abbreviations of the climate, land use class, and vegetation type separated by a dash. Wheat is also shown here to emphasize its importance for the total arable land class.

This chapter is structured as follows. In the method section, we update the deposition parameters to describe the stomatal resistance, the roughness length and growing season. In the results section, we inspect the total dry deposition of NH_x and NO_y and their effect on the PM2.5 formation and concentration of ammonium and nitrate. We conclude with some closing remarks.

Table 1: The updated vegetation types in the temperate climate (tmp) within land use classes arable land (ara) and semi-natural vegetation (sem). Note: wheat is not updated, because the default arable land class was considered to be wheat.

Climate zone	Land use	Vegetation	Description
Tmp	Ara	Whd	Wheat (default)
Tmp	Ara	Maz	Maize
Tmp	Ara	Rpd	Rapeseed
Tmp	Ara	Brd	Barley
Tmp	Ara	Sfw	Sunflower
Tmp	Ara	Oad	Oats (default)
Tmp	Ara	Fcl	Fodder Crops (cereal)
Tmp	Ara	Sug	Sugar Beet
Tmp	Sem	Shr	Shrubland
Tmp	Sem	Ngr	Natural Grassland

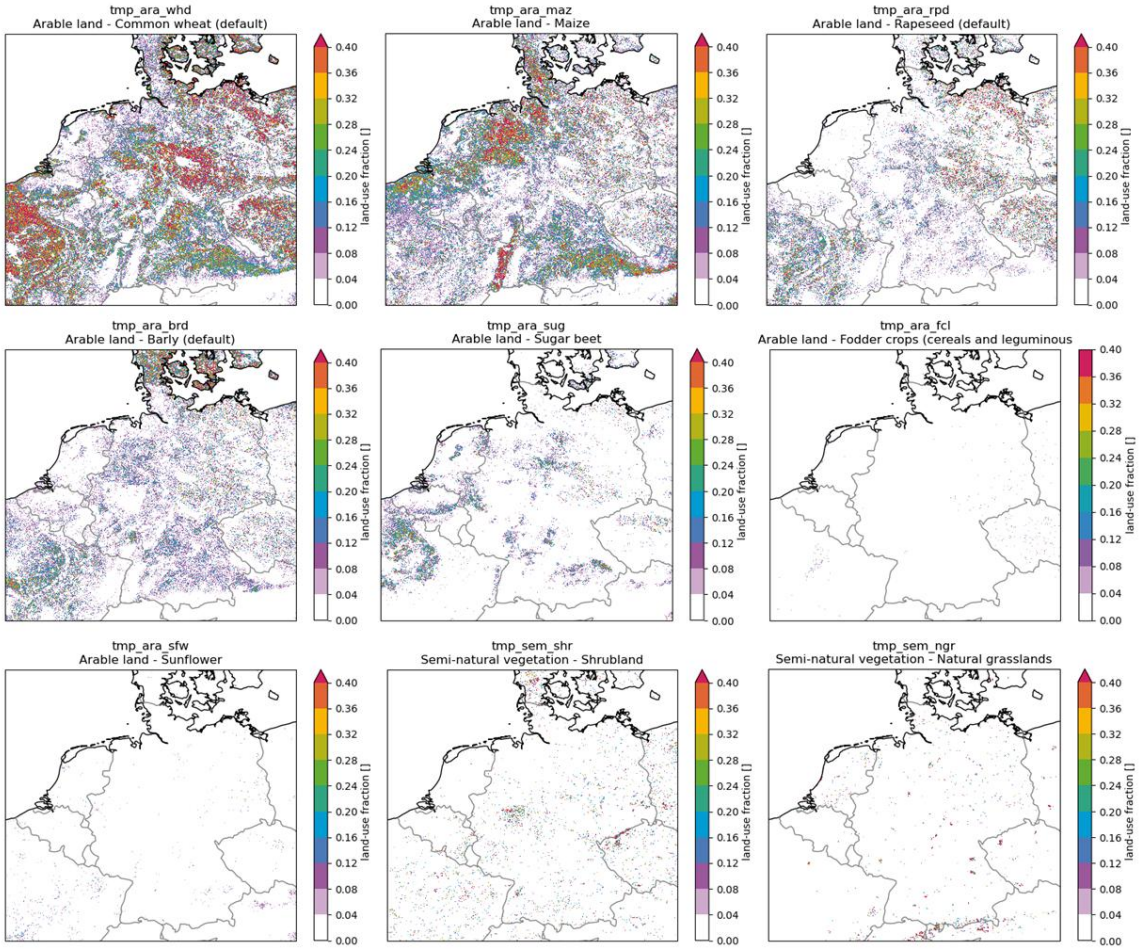

Figure 4: The land use fraction maps of (top) wheat, maize, rapeseed, and (middle) barley, sugar beet, fodder, (bottom) sunflower, shrubland, and natural grassland.

4.2 Methods

4.2.1 Detailing vegetation dry deposition parameters

In this work, three classes of dry deposition parameters are detailed that define the stomatal conductance and the roughness length, and the growing season Sections 4.2.1.1 and 4.2.1.2, respectively.

4.2.1.1 Stomatal Conductance and Roughness Length

Whenever available from literature, the updated dry deposition parameters are: the optimal, minimal, and maximal temperatures for stomatal opening T_{opt}, T_{min}, and T_{max}, the minimum and maximum vapor pressure deficit vpd_{min} and vpd_{max}, the maximum leaf stomatal conductance gs_{max}. For the latter, conductance for ozone is used as the international reference. The updated parameters for the arable land and semi-natural land are listed in Table 2.

The larger the stomatal conductance gs_{stom}, the higher the dry deposition via the stomatal pathway. The gs_{stom} is defined as

$$gs_{\mathrm{stom}} = \mathrm{LAI} \cdot gs_{\max} \cdot f_{\mathrm{light}} \cdot f_{\mathrm{temp}} \cdot f_{\mathrm{vpd}} \cdot f_{\mathrm{sm}}$$ **Equation 4.1**

where LAI is the leaf area index, gs_{max} is the maximum stomatal conductance, and the f parameters are correction factors between 0 and 1. The f_{light} corrects for the amount of sunlight or shade reaching the leaves, f_{temp} is a bell shaped curve being zero at T_{max} and T_{min}, and one at T_{opt}, f_{vpd} is a function which is one for vpd below $vpd_{min,}$ it is zero for vpd above $vpd_{max,}$ or it is a linear interpolation between 1 and f_{min}. The f_{sm} is a correction factor related to the soil moisture index.

The full-grown vegetation height *h* is an important parameter defining the roughness length. The roughness length in turn defines the aerodynamic resistance R_a and applies to the dry deposition of all species. Effectively, increased full-grown vegetation heights lead to increased dry deposition of all species including gaseous species and aerosols.

Table 2: The dry-deposition parameters defining the stomatal conductance and roughness length on arable and semi-natural vegetation classes. Values that are improved are shown in bold with their references are given in the footnotes.

land use	Vegetation	T_{min}	T_{opt}	T_{max}	h	vpd_{min}	vpd_{max}	f_{min}	gs_{max}
Ara	Def (Whd)	12.0	26.0	40.0	1.0	2.8	0.9	0.01	0.0073171
Ara	Maz[1] [2] [3]	**5.0**	**25.0**	**35.0**	**2.8**	2.8	0.9	0.01	**0.003659**
Ara	Rpd[4] [5] [6]	**5.0**	**22.0**	**39.0**	1.0	**3.5**	**1.5**	**0.02**	**0.01195**
Ara	Brd[7] [8]	**5.0**	**16.5**	40.0	**0.75**	**3.0**	**1.0**	0.01	**0.009268**
Ara	Sfw[9]	12.0	26.0	40.0	**2.0**	2.8	0.9	0.01	0.0073171
Ara	Oad	12.0	26.0	40.0	1.0	2.8	0.9	0.01	0.0073171
Ara	Fcl	12.0	26.0	40.0	1.0	2.8	0.9	0.01	0.0073171
Ara	Sug[10]	12.0	26.0	40.0	**0.35**	2.8	0.9	0.01	0.0073171
Sem	Def	8.0	24.0	39.0	0.2	4.5	2.8	0.04	0.010244

[1] Ref. (Taube et al., 2020)
[2] Ref. (Sinsawat et al., 2004)
[3] Ref. (Melkonian, 2004)
[4] Ref. (Op de Beeck et al., 2010)
[5] Ref. (Raboanatahiry et al., 2021)
[6] Ref. (Ghassemi-Golezani et al., 2024)
[7] https://www.teagasc.ie/media/website/publications/2015/The-Spring-Barley-Guide.pdf
[8] https://ahdb.org.uk/knowledge-library/measurement-of-stem-extension-and-stem-reserves-in-barley
[9] https://www.bolster.eu/sunflower-large-flowered-helianthus-annuus/p176
[10] https://www.fertiglobal.com/cmp/sugar-beet-program/

land use	Vegetation	T_{min}	T_{opt}	T_{max}	h	vpd_{min}	vpd_{max}	f_{min}	gs_{max}
Sem	Shr [11] [12]	**-5.0**	**15.0**	**40.0**	0.2	4.5	**1.75**	**0.1**	**0.005122**
Sem	Ngr [11] [12]	**5.0**	**25.0**	**45.0**	**0.1**	4.5	**1.75**	**0.1**	**0.004634**

4.2.1.2 Growing Season

The DEPAC description of the LAI has the following form:

$$\mathrm{LAI}(t) = \begin{cases} \mathrm{LAI}_{\min} & \text{if } t \le t_{\mathrm{sg}} \vee t \ge t_{\mathrm{ed}} \\ \mathrm{LAI}_{\min} + (t - t_{\mathrm{sg}})\Delta\mathrm{LAI}_{\mathrm{growth}} & \text{if } t_{\mathrm{sg}} < t \le t_{\mathrm{eg}} \\ \mathrm{LAI}_{\max} & \text{if } t_{\mathrm{eg}} < t < t_{\mathrm{sd}} \\ \mathrm{LAI}_{\max} + (t - t_{\mathrm{sd}})\Delta\mathrm{LAI}_{\mathrm{decay}} & \text{if } t_{\mathrm{sd}} \le t < t_{\mathrm{ed}} \end{cases}$$

Equation 4.2

$$\Delta\mathrm{LAI}_{\mathrm{growth}} = (\mathrm{LAI}_{\max} - \mathrm{LAI}_{\min})/\mathrm{SLEN}$$
$$\Delta\mathrm{LAI}_{\mathrm{decay}} = (\mathrm{LAI}_{\min} - \mathrm{LAI}_{\max})/\mathrm{ELEN}$$

Equation 4.3

where LAI_{min} and LAI_{max} are the minimum and maximum LAI, ΔLAI_{growth} and ΔLAI_{decay} are the LAI growth and decay rate and SLEN and ELEN the length of the growing and decay period, respectively. The t_{sg} and t_{eg}, and t_{sd} and t_{ed} are the start and end of the growing and decay season, respectively, which depend on the latitude λ:

$$t_{\mathrm{sg}}(\lambda) = \mathrm{SGS}_{50} + \mathrm{D}_{\mathrm{SGS}}(\lambda - 50^{\circ})$$
$$t_{\mathrm{eg}}(\lambda) = t_{\mathrm{sg}}(\lambda) + \mathrm{SLEN}$$
$$t_{\mathrm{sd}}(\lambda) = t_{\mathrm{ed}}(\lambda) - \mathrm{ELEN}$$
$$t_{\mathrm{ed}}(\lambda) = \mathrm{EGS}_{50} + \mathrm{D}_{\mathrm{EGS}}(\lambda - 50^{\circ})$$

Equation 4.4

where SGS_{50} and EGS_{50} are the start of the growth/decay season at 50ºN degrees latitude, and D_{SGS} and S_{EGS} is the shift of the growth/decay season per degree latitude away from 50ºN. For vegetation on arable land and semi-natural land, the D_{SGS} and S_{EGS} are set to zero.

For vegetation on arable land, the plant growth goes through the stages: dormancy, emergence, ripening and harvesting which correspond to the four stages from top to bottom written in the LAI equation. We assume the ripening period ($t_{eg} < t < t_{sd}$) to be 50 days and harvesting ($t_{sd} < t < t_{ed}$) takes place in 7 days for all vegetations on arable land. Then, given the day of the start of the emergence t_{sg}, and the start of the harvesting t_{sd}, all LAI growth parameter can be derived. The growing season of the seminatural shrubland is taken as the deciduous shrub class and the natural grassland as the long grass class from (Zhang et al., 2003). The updated growth and decay of the leaf area index based on the parameters listed in Table 3 are shown in Figure 5.

4.2.2 Simulation Details

The impact of the functional changes was investigated by LOTOS-EUROS v3.0.000 simulations over 2019 with a spin-up period of one month. First, a simulation over Europe on

[11] Ref. (Zhang et al., 2003)
[12] https://icpvegetation.ceh.ac.uk/sites/default/files/Chapter%203%20-%20Mapping%20critical%20levels%20for%20vegetation.pdf

a resolution of ~20 x 20 km^2 has been used for nesting the model (W15-E35; N35-N70, 0.5x0.25º resolution). Subsequently, the model was run at a resolution of ~6 x 6 km^2 for the domain of Northwest Europe (E2-E16; N47-N56, 0.1x0.05º resolution) to test and compare the functional changes.

All simulation include the EU emission inventory CAMS-REG v5.1 (Kuenen, et al., 2022) for the year 2018 of submission year 2021, and for Germany, the Greta emission inventory v1.2.0.1 from 2019 from submission year 2022 (Umweltbundesamt, 2022). Biogenic emissions using tree-specific emission factors, soil-NOx emissions, sea salt emissions, desert dust, road resuspension and agricultural dust emissions and GFAS wildfire (Kaiser et al., 2012) emissions were used. Climatological boundaries from EMEP, Isaacson and Logan are used together with 3-hourly results from the CAMS-nrt product. This basically implies that for the most important tracers, the CAMS-nrt product is used. Additionally, time profiles from TEMPO v3.2 (Guevara et al., 2025) are used. These profiles have a detailed profile specified per country and sector.

The simulation as described above using default values for the arable land and semi-natural land is called the reference run throughout the report. In this chapter, the simulation including the detailing of the vegetation parameters called the test run.

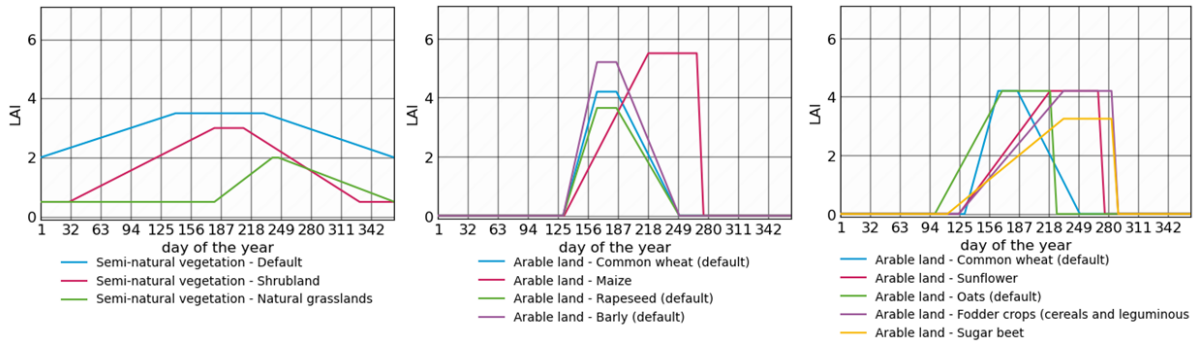

Figure 5: The leaf area index (LAI) defined by Equation 4.2 to Equation 4.4 and deposition parameters in Table 3.

Table 3: The leaf area index growth parameters classes that are improved are shown in bold. The references are given in the footnotes.

land use	Vegetation	SGS_{50}	SLEN	EGS_{50}	ELEN	LAI_{min}	LAI_{max}
Ara	Def	130	35	250	65	0.0	4.2
Ara	Maz[13] [1]	**131**	**87**	**275**	**7**	0.0	**5.5**
Ara	Rpd[14]	130	35	250	65	0.0	**3.65**
Ara	Brd[7]	130	35	250	65	0.0	**5.2**
Ara	Sfw[13]	**124**	**95**	**276**	**7**	0.0	4.2
Ara	Oad[13]	**99**	**70**	**226**	**7**	0.0	4.2
Ara	Fcl[13]	**124**	**109**	**290**	**7**	0.0	4.2
Ara	Sug[13] [15]	**112**	**121**	**290**	**7**	0.0	**3.25**
Sem	Def	0	140	366	135	2.0	3.5
Sem	Shr[11]	**30**	**150**	**330**	**120**	**0.5**	**3.0**
Sem	Ngr[13]	**180**	**60**	**366**	**120**	**0.5**	**2.0**

4.3 Results

Table 4 lists the nitrogen dry deposition fluxes of the adjusted land use-vegetation class and the reference system with default arable land and semi-natural land. The largest impact is found for Maize (470), Sunflower (457), and Fodder crops (447), while the reference have values of 431 eq N ha^{-1} yr^{-1}. This is because maize has a much larger height, higher maximum LAI and longer growing season compared to the default shown in Table 2 and Table 3. For sunflower and fodder crops, the growing season has been extended (Figure 5) and the height of sunflowers has been increased. The impact on barley and rapeseed is considerably smaller, as their updated vegetation parameters balance each other out. For rapeseed, gs_{max} is increased, but LAI_{max} is decreased. For barley, LAI_{max} and gs_{max} have increased, but its height has decreased. On the semi-natural land, shrubland shows slightly higher values (415) compared to 405 Eq N ha^{-1} yr^{-1} for the default class. For the changes of Lai_{max}, LAI_{min} and gs_{max} a decrease in dry deposition is expected. On the other hand T_{opt}, $T_{min,}$ and T_{max} are closer to actual temperatures in Germany, which will cause an increase of deposition for this class.

[13] Ref. (DWD Climate Data Center, 2024)
[14] Ref. (Sun et al., 2021)
[15] Ref. (Jay et al., 2017)

Overall it turns out that shrubland is slightly larger compared to the default. Natural grassland shows lower average dry deposition compared to the default of 405 Eq N ha^{-1} yr^{-1}. Here the changes for gs_{max}, LAI_{max}, and LAI_{min} result in lower deposition, while other values are unchanged. So the overall decrease is as expected.

Figure 6 shows the maps and the relative difference of the NH_x and NO_y dry deposition. For NO_y deposition, we observe an increase throughout the domain which is explained by the updated parameters for barley, maize and rapeseed. As the daily average concentrations of the NO_y species are relatively constant throughout the year, inspecting the area under the LAI curve provides a rough estimate of the impact on the deposition which for barley, maize and rapeseed all show increased LAIs. In addition, barley and rapeseed increases their gs_{max} and maize increases its height h, with respect to the default, which all lead to increased deposition of NO_y.

There are various areas with decreased NO_y dry deposition, for example, in Czechia and Denmark which coincides with regions of decreased NH_x deposition. In contrast to NO_y, the average daily concentration of NH_3 peaks in spring due to the manure application on arable land. Therefore, the dry deposition is most sensitive to changes in this time period. In the north west of Germany where high concentration of NH_3 are measured, we observe lower NH_x deposition with the updated deposition parameters. In this region, maize and rapeseed both have a slower growth of its LAI compared to the default (see Figure 5). In the time period of high NH_3 concentrations, maize and rapeseed are thus less effective in absorbing NH_3 compared to the default leading to lower dry depositions. As a result, NH_3 will be transported over longer distances and deposit elsewhere.

Table 4 The averaged dry deposition flux N per land use class of the reference, and the test run with updated vegetation parameters. Units are in Eq. N ha^{-1} yr^{-1}. Averages taken are over Germany.

Land use code	Vegetation code	Reference	Update
Ara	Ref	431	432
Ara	Whd	431	432
Ara	Maz	431	470
Ara	Rpd	431	429
Ara	Brd	431	428
Ara	Sfw	431	457
Ara	Oad	431	432
Ara	Fcl	431	447
Ara	Sug	431	427
Sem	Ref	405	405
Sem	Shr	405	415
Sem	Ngr	405	389

A second effect that plays a role in the (effective) dry deposition of NH_3 is re-emission from the soil, stomata and external leaf surfaces which act as a NH_3 reservoir. Especially, after the NH_3 concentration peak when the concentrations are relatively low, NH_3 can be re-emitted to

the air. In the case of maize for which LAI_{max} is increased in this time period, the rate of re-emission is increased, contributing to lower (effective) dry deposition.

Finally, we analyze the effect on the PM2.5 concentrations of nitrate and ammonium in Figure 7. The relative change of ammonium and nitrate PM2.5 concentrations show the same pattern as they are formed from NH_3 and NO_2. Naturally, these patterns are closely related to the NH_x and NO_y deposition as in regions where there is less deposition of both NH_x and NO_y, ammonium and nitrate aerosols have the opportunity to form such as in Denmark and Czechia. Conversely, in regions where the concentration of one of the two species decreases, e.g. by increased deposition, the formation of ammonium and nitrate is suppressed as seen throughout Germany.

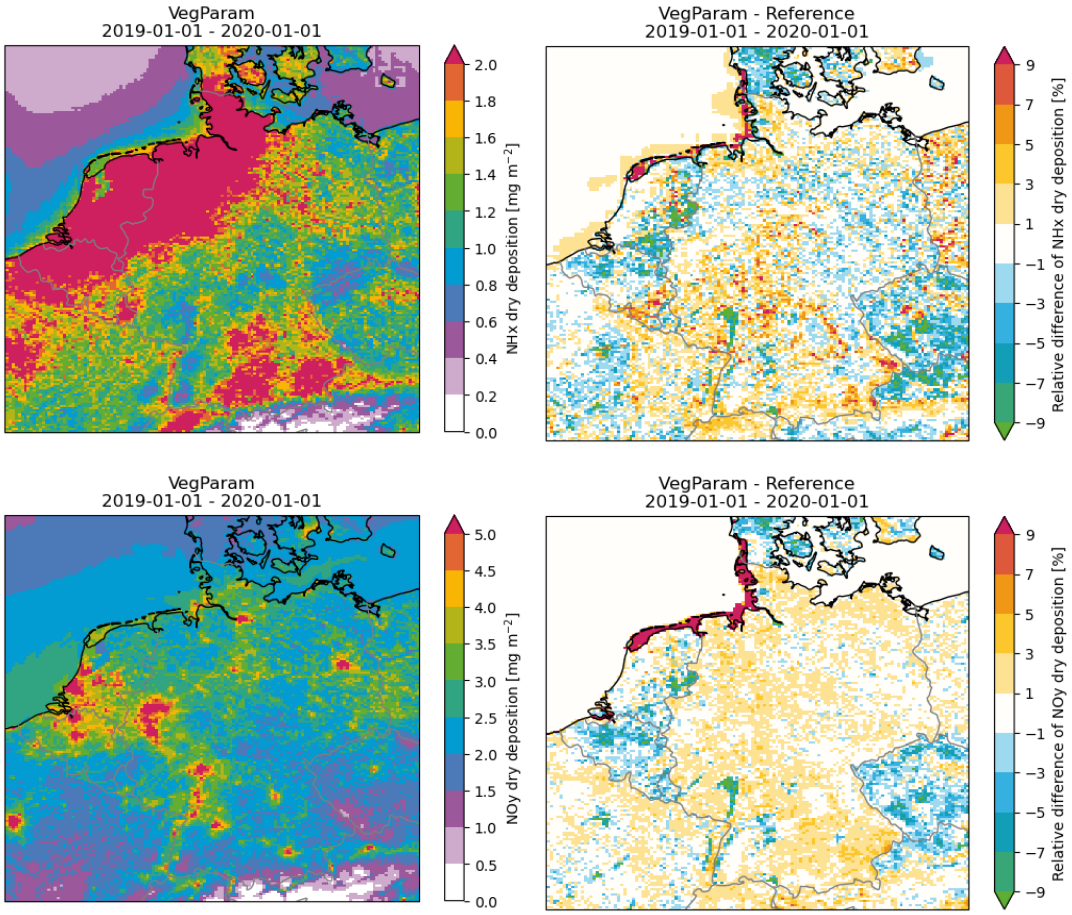

Figure 6: The maps (left) and relative difference (right) of the NHx (top) and NOy (bottom) dry deposition. In the relative difference plots, the green to red color scale mean that in the test run VegParam, there is less to more dry deposition compared to the reference run, respectively.

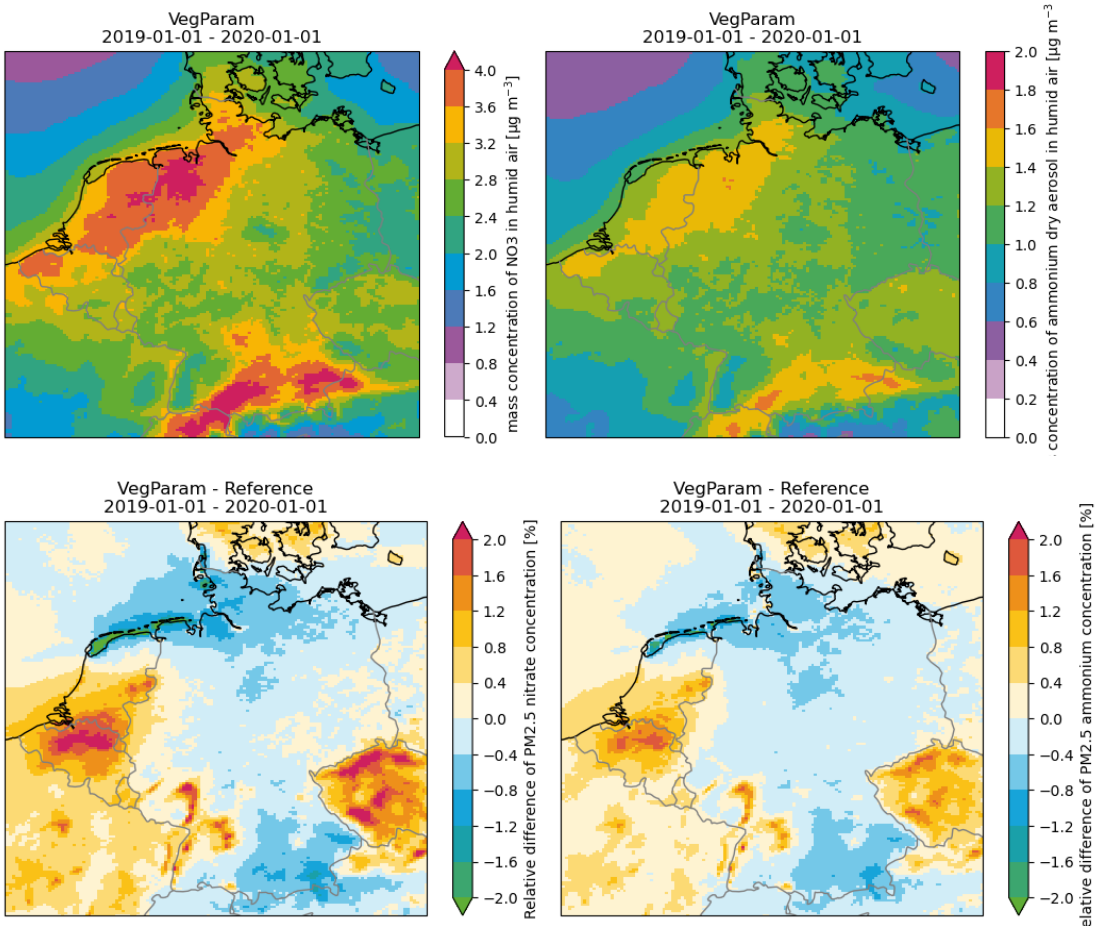

Figure 7: The maps and relative difference with respect to the reference of aerosol (PM2.5) concentrations of nitrate and ammonium in humid air of the test run.

4.4 Conclusions

This work focused on improving dry deposition parameters by detailing vegetation specific parameters leveraging our new Three-Tiered Land Use Approach. We updated parameters that define the dry deposition though stomatal and external leaf surfaces and the growth season of the dominant vegetation classes on arable land and semi-natural land in northwest Europe. For NO_y, as the daily averaged concentration profile is relatively constant throughout the year, the total growth season defined by the LAI is more important compared to its shape (e.g., the timing of the start of the growing season). In contrast, for NH_x the temporal profile of NH_3 concentration is essential to understand the observed behavior. A high concentration peak in spring due to manure application can be “missed” by a delayed growing season of the local vegetation. Specifically maize, which is the dominant adapted land use class, has been given a slower growth of LAI leading to decreased NH_x depositions. We additionally inspected the aerosol PM2.5 formation of ammonium and nitrate, naturally closely related to each other and to the dry deposition of NH_x and NO_y. In the regions where both NH_x and NO_y deposition is increased, we observe a decrease of nitrate and ammonium and vice versa.

5 Satellite-derived forest Leaf Area Index

5.1 Introduction

An important pathway of the dry deposition of nitrogen-containing components is via the uptake through the stomata of leaves. As more leaves lead to increased nitrogen (N) dry deposition, the amount of leaves, captured by the leaf area index (LAI) is an important parameter in the model. The leaf area index (LAI) is a dynamic vegetation parameter that expresses the ratio between the (one-sided) area of leaves per unit area (m^2/m^2) and typically lies between zero and seven.

In DEPAC (van Zanten et al., 2010), the deposition model implemented in LOTOS-EUROS, the LAI is parameterized in a straightforward and elegant manner. However, it lacks consideration for temporal effects and only minimally incorporates spatial dependencies. Therefore, this work aims to enhance the spatial and temporal description of the LAI of trees by utilizing satellite-derived LAI data combined with a high-resolution tree map.

For that, we start by inspecting GEOV2, a processed MODIS LAI dataset available from 1999 -2020 on a 1x1km resolution (Verger et al., 2023), on its variability in time and space. We aim to see temporal effects such as drought, excessive rain, cold and long winters and spatial dependencies on the growth and decay of the LAI. Then, the satellite-derived LAI dataset is prepared to be read by LOTOS-EUROS to perform a sensitivity analysis. The NH_x and NO_y dry deposition and nitrate and ammonium aerosol concentrations are inspected and compared to the reference simulation that use the forest LAI description of DEPAC.

This section of the report is structured as follows. First, in the method section the DEPAC forest LAI is shown. Then, the GEOV2 dataset and tree density map are introduced and we explain how we constructed the broadleaf and coniferous tree LAI. Second, the results and discussions are separated into two parts: the satellite-derived LAI, and the LOTOS-EUROS sensitivity runs. We close with conclusions and suggested improvements.

5.2 Methods

5.2.1 Leaf Area Index

Section 4.2.1.2 describes the LAI in DEPAC. Here, in Table 5 the LAI parameters of deciduous and coniferous trees as defined in DEPAC, from now on called default LAI, are listed and Figure 8 shows the default LAIs at 48.2 degrees N.

Table 5: DEPAC default LAI parameters for deciduous and coniferous trees including their units.

	LAI_{min}	LAI_{max}	SGS_{50}	SLEN	EGS_{50}	ELEN	D_{SGS}	D_{EGS}
units	m^2/m^2	m^2/m^2	m^2/m^2/day	m^2/m^2/day	day	day	day/ºN	day/ºN
deciduous forest	0	4.0	20	30	100	307	1.5	-2.0
coniferous forest	5.0	5.0	1	1	0	366	0	0

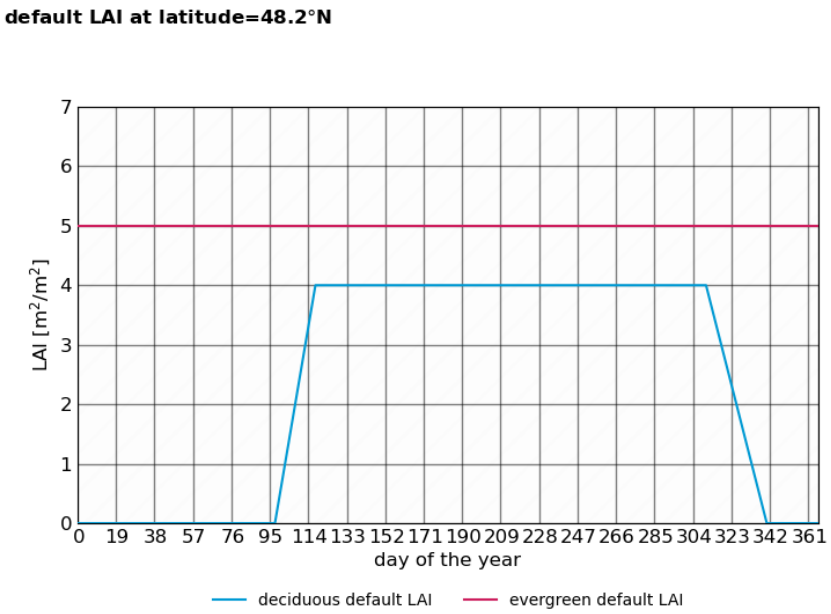

Figure 8: The DEPAC (default) LAI of the broadleaf (deciduous) and coniferous (evergreen) LAI at 48.2 degrees N

5.2.2 Constructing broadleaf and coniferous tree satellite-derived LAI

The GEOV2 dataset provides an improved time series of LAI at 1 km spatial resolution, covering the period from 1999 to 2020 (Verger et al., 2023). The applied smoothing techniques help reduce noise from cloud cover and atmospheric disturbances, ensuring a more reliable representation of seasonal and long-term vegetation trends.

The high resolution tree map is a dominant tree map from 2018 of three types: no trees, broadleaved, and coniferous trees. The map is on a 10m raster and provided by the Copernicus Land Monitoring Service (Forest Type 2018 (raster 10 m, 100 m), Europe, 3-yearly — Copernicus Land Monitoring Service, 2025). In this dataset, agricultural trees and urban trees are removed.

The satellite-derived LAI is constructed taking the following steps:

- Extract forest LAI from satellite data using tree map masks.
  1. Create tree masks of the coniferous and broadleaf tree on a 1x1km grid and select cells with >90% tree density. The 90% minimum fraction is chosen such that the satellite-derived LAI is “polluted” as little as possible with other land use classes such as grass, or crops, while still representing the area.
  2. Overlay the tree masks on the satellite-derived LAI dataset.
- Rescale the LAI to retrieve deciduous and evergreen forest properties.
  1. Divide the domain in blocks, and average the LAI over space in each block.
  2. Perform a rescaling for each block for each year. Note: the rescaling will be explained in the Results section.
  3. Finally, the lon, lat, time-dependent LAI_{LE} is saved to a netcdf-file to be read by LOTOS-EUROS. The lon, lat-dependency of LAI_{LE} is now defined by the blocks.

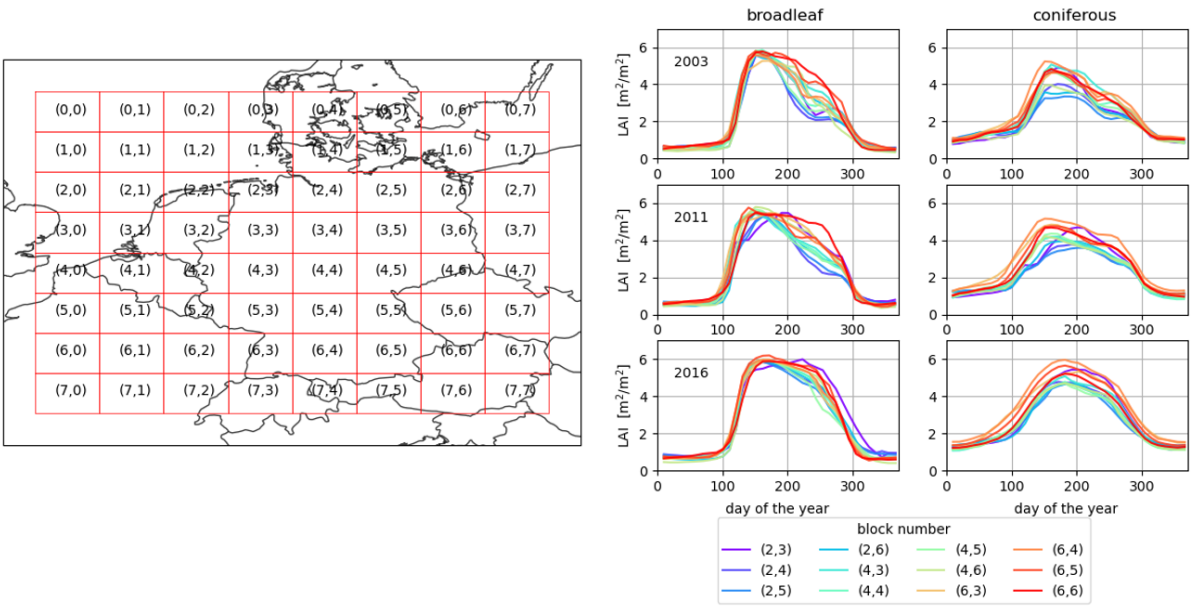

Figure 9: (left) The domain is divided into blocks numbered (0,0) to (7,7). (right) In each block, the temporal LAI is averaged and scaled per year. The averaged broadleaf and coniferous tree GEOV2 satellite-derived LAI in various blocks throughout Germany in 2003, 2011 and 2016. Purple to red colors range from the north to south Germany, respectively.

5.2.3 Simulation Details

In Section 4.2.2, the refences simulation is described in detail and is run with the default LAI parameters listed in Table 5. In this chapter in the test simulation, the LAI of the broadleaf and coniferous forest which' land use fraction is shown in Figure 10, is replaced by the rescaled satellite-derived LAI based on Verger et al., 2023.

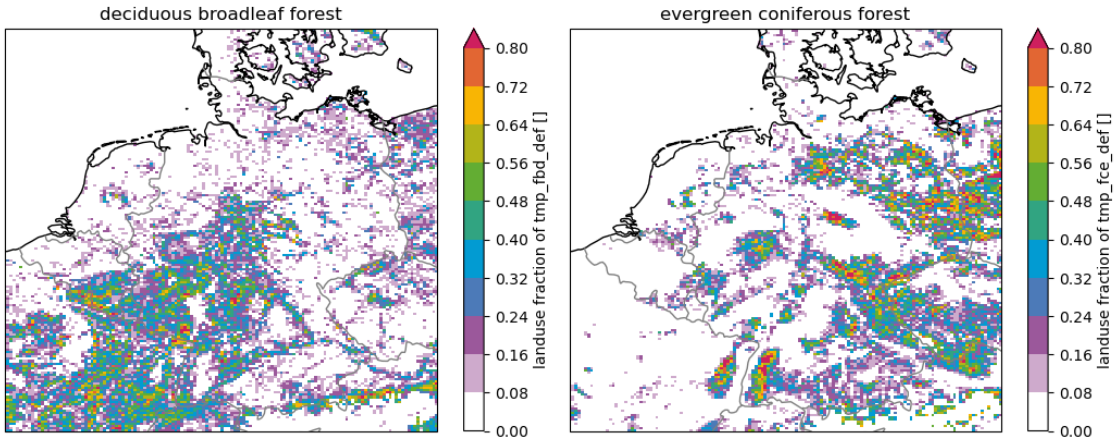

Figure 10 The land use fraction map of the deciduous broadleaf and evergreen coniferous forest.

5.3 Results

This results section is composed of two parts. First, the spatial and temporal variability of the satellite-derived LAI is assessed. Second, the sensitivity of the LAI on nitrate and ammonium aerosols are tested in LOTOS-EUROS.

5.3.1 Temporal and Spatial Variations in MODIS LAI

The satellite-derived LAI shows both spatial and temporal variability in the domain as shown in Figure 9. The broadleaf trees LAI in all years shows in the south of Germany, e.g. blocks (6,3), (6,4), (6,5), and (6,6) in the orange to red colors, a much longer plateau of high LAI values in the summer compared to the north of Germany e.g. in blocks (2,3), (2,4), and (2,5) in the purple to blue colors. For the coniferous trees LAI, the maxima in the south are higher compared to the maxima in the north. In addition, the temporal effects are also visible in the dataset. For example, the heat wave in Europe in 2003, the excessive rain fall in 2011 results in a fast and early decay of broadleaf tree LAI compared to a “normal” year in 2016. However, for the coniferous trees LAI, the effects are less visible.

The satellite-derived LAI is not able to show the seasonality of the two tree types correctly which is a known problem seen over multiple satellite-derived LAI datasets. Most broadleaf trees in Northwest Europe are deciduous and in the winter do not have leaves i.e. LAI=0. However, the satellite-derived LAI converges to LAI=0.5-1.0 in the winter months. Additionally, most coniferous trees in Northwest Europe are evergreen, but the satellite-derived LAI shows a large change from the winter (LAI=1.0-1.5) compared to the summer (LAI=3.0-5.0).

To correct for this seasonality and construct a LAI for deciduous and evergreen forests for LOTOS-EUROS, a rescaling of the satellite-derived LAI is performed. The minimum of the deciduous tree LAI is shifted to zero and the LAI is renormalized to its satellite-derived maximum LAI value in each year such that the LAI in the winter is zero but keeps the maximum LAI in the summer. For evergreen trees, we use the satellite-derived maximum LAI value for each block and each year, assuming no seasonal variability between winter and summer. Although temporal variability in LAI could be expected for evergreen species, we adopt this simplified approach due to the lack of (experimental) data necessary to accurately quantify such variability.

For each year separately, in each block, the satellite-derived LAI is rescaled by:

$$\mathbf{LAI_{LE}}(\mathbf{t},\mathbf{lon},\mathbf{lat}) = \begin{cases} (\mathbf{LAI} - \min_{\mathbf{t}}\mathbf{LAI})\,\frac{\max_{\mathbf{t}}\mathbf{LAI}}{\max_{\mathbf{t}}\mathbf{LAI} - \min_{\mathbf{t}}\mathbf{LAI}}, & \text{deciduous trees} \\ \max_{\mathbf{t}}\mathbf{LAI}, & \text{evergreen trees} \end{cases} \qquad \textbf{Equation 5.1}$$

where t is time in the selected year, the blocks can be selected by lon and lat, and LAI_{LE} is the rescaled LAI that is read in by LOTOS-EUROS. Note that for readability, the dependency of the satellite-derived LAI on time, longitude and latitude is not explicitly written on the right hand side of the equation.

The resulting broadleaf tree LAI is shown in Figure 11 with all years shown in a grey, except the years 2003 and 2011 shown in red. This figure highlights both spatial and temporal effects. Notably, the 2003 drought had a more pronounced impact on LAI in west Germany compared to the east. Additionally, the warm spring of 2011 shifts the start of the growing season to the earliest times observed, while the dry spring of 2003 delayed the growing season by 10-20 days. Furthermore, the difference between the default LAI and the rescaled satellite-derived LAI is clearly visible. In the late spring/beginning of the summer, the LAI_{LE} is higher than the default, peaking up to 6, while in late summer/fall, the LAI_{LE} significantly decays earlier and slower. The growth rate, and the end of the decay season are similar for both.

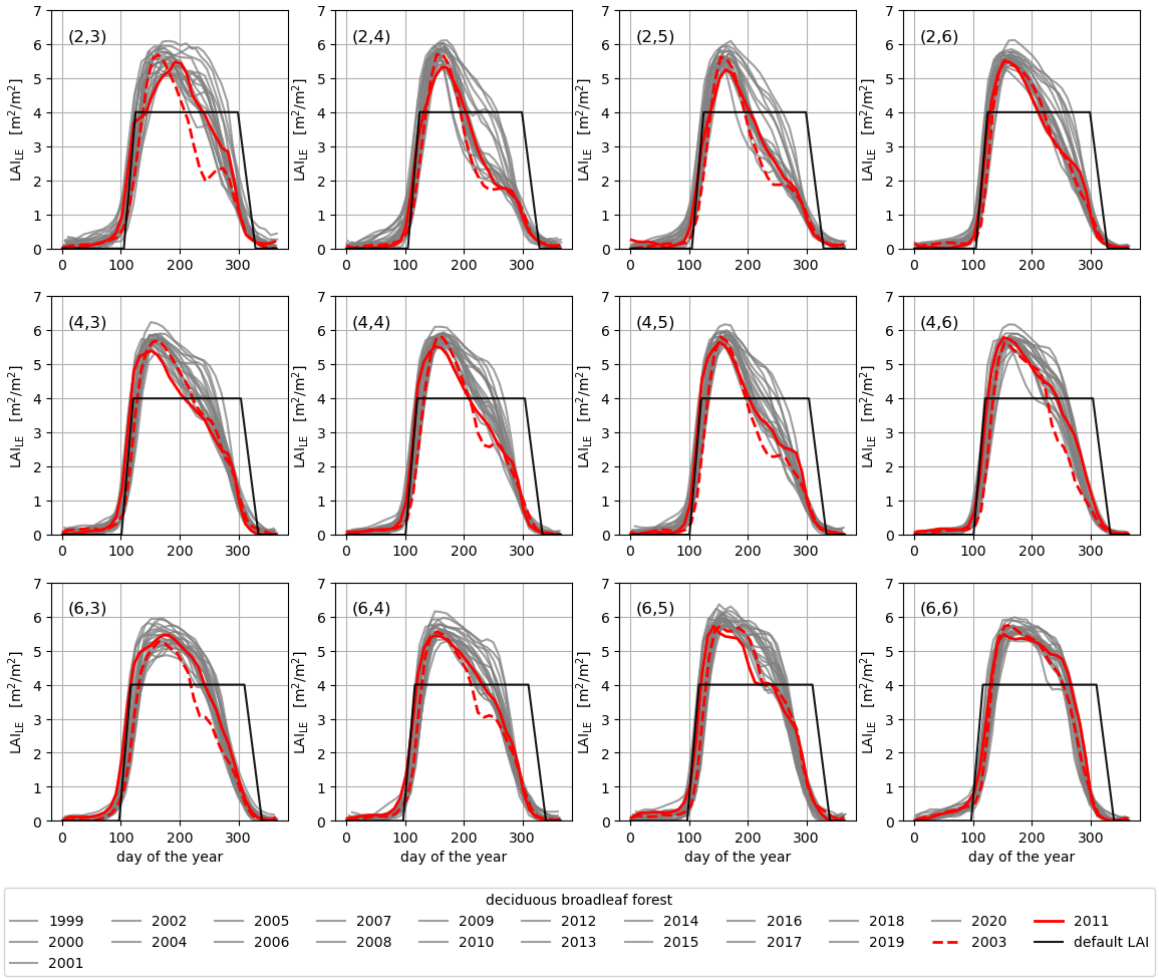

Figure 11: The rescaled broadleaf deciduous satellite-derived LAI in various regions in Germany as indicated by the block numbers in each figure. All years from 1999-2020 are shown in grey, except 2003 which had a warm summer and 2011 which had a warm spring and winter and excessive rainfall in the summer shown in red.

5.3.2 Sensitivity Analysis

To test the effect of the rescaled satellite-derived LAI on the NH_x and NO_y dry deposition and ammonium and nitrate aerosol concentration, sensitivity runs using LOTOS-EUROS are performed for the year 2019. In Figure 12, the broadleaf deciduous and coniferous evergreen LAI_{LE} that is used in the test-run are shown. Note that in the land use fraction map, there are no coniferous deciduous and broadleaf evergreen forests.

Figure 13 shows the total, i.e. dry and wet, deposition flux of NH_x and NO_y of the sensitivity test run, and their ratio. Overall, the NH_x and NO_y deposition over Germany decreases from 634 to 625 and 326 to 321 Eq ha^{-1} yr^{-1} by the use of LAI_{LE}, respectively.

In the northeast, there are predominantly coniferous trees which show up to 10% less NH_x and NO_y deposition in the ratio plot (Figure 13). As the coniferous default LAI and LAI_{LE} are constant throughout the year, a simple inspection of their LAI ratio or the area under their LAI curve explains the observed changes in dry deposition. Namely, in the northeast, coniferous tree LAI_{LE}<default LAI and thus explains the reduced dry deposition of both NH_x and NO_y. The ratio plots in Figure 14 confirm the dependency of the dry deposition flux on the trends of the

LAI for coniferous evergreen forest, namely, that the northeast shows less dry deposition compared to the southwest of Germany.

The ratio plots in Figure 14 display a checkerboard pattern, which results from the way the spatial variation is incorporated in LAI_{LE} by distinguishing only between coniferous and broadleaf trees and spatially averaging in each block. To improve the representation of tree types and avoid the checkerboard effect, a more detailed sampling approach based on individual tree species is recommended. This would enhance the ability to capture spatial variability in LAI. Moreover, temporal variability in LAI, influenced by the tree's response to heat and drought, is also strongly correlated with species type.

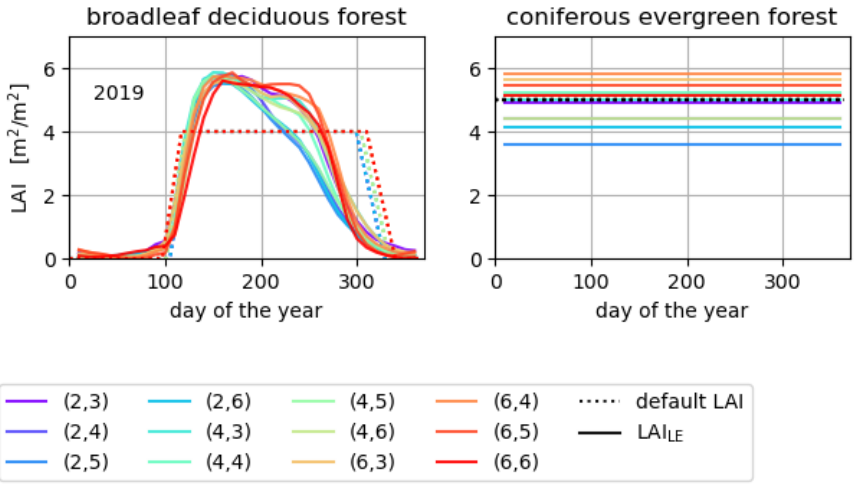

Figure 12: The broadleaf deciduous and coniferous evergreen LAI_{LE} as implemented in the LOTOS-EUROS sensitivity runs over the year 2019. The solid lines are the rescaled satellite-derived LAIs and the dotted lines the default DEPAC LAIs. The colors represent the various locations in Germany, while the coniferous default LAI is colored black as it is not location-dependent.

In the southwest of Germany, broadleaf trees are prevalent (Figure 10). A direct comparison between the area under the LAI curves and dry deposition rates is not possible, as deciduous trees exhibit strong seasonal variation. As explained in section 4.3, the NH_x deposition is mainly influenced by the ammonia concentration peak in spring. In spring, the broadleaf deciduous LAI_{LE}<default LAI as the satellite data shows a delayed start of the growth season compared to DEPAC (Figure 12) contributing to the observed effect of less NH_x deposition over the full domain (Figure 14). In addition, although the broadleaf tree LAI_{LE}>default LAI in the summer months, summer of 2019 was exceptionally warm which leads to the closing of stomata to protect the tree from drought. Closing of the stomata happens the for broadleaf trees at T_{max}=35 degrees Celsius, and blocks N-uptake and thus prevents the dry deposition of N-compounds through the stomata. Effectively, we observe less dry NO_y and NH_x deposition in this region (Figure 13), albeit for different reasons and timing compared to the northeast.

Finally, the PM2.5 nitrate and ammonium concentration changes are shown in Figure 15. Both species show an overall increase of up to 2% in central and south Germany, coinciding with the observed decrease of NH_x and NO_y dry deposition.

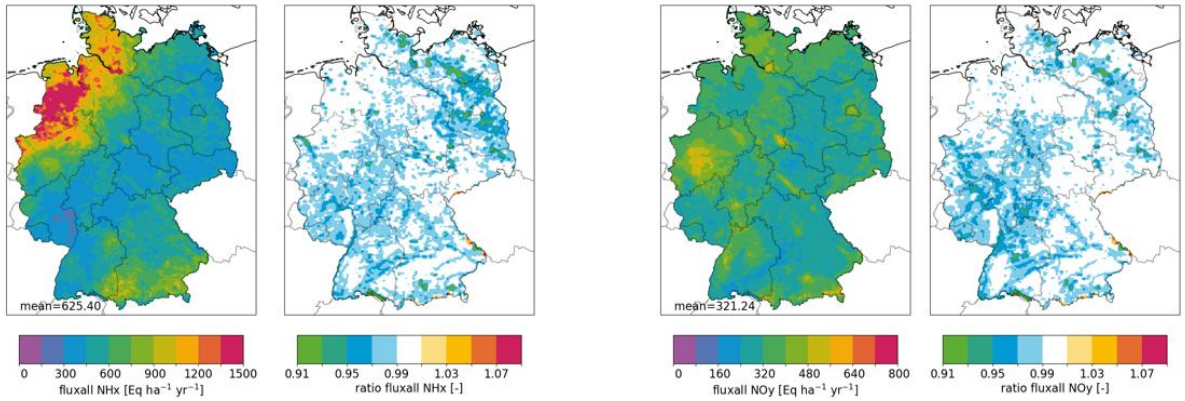

Figure 13: From left to right: total deposition flux of NH_x of the rescaled satellite-derived LAI_{LE} and its ratio with the reference, total deposition flux of NO_y of the rescaled satellite-derived LAI_{LE} and its ratio with the reference.

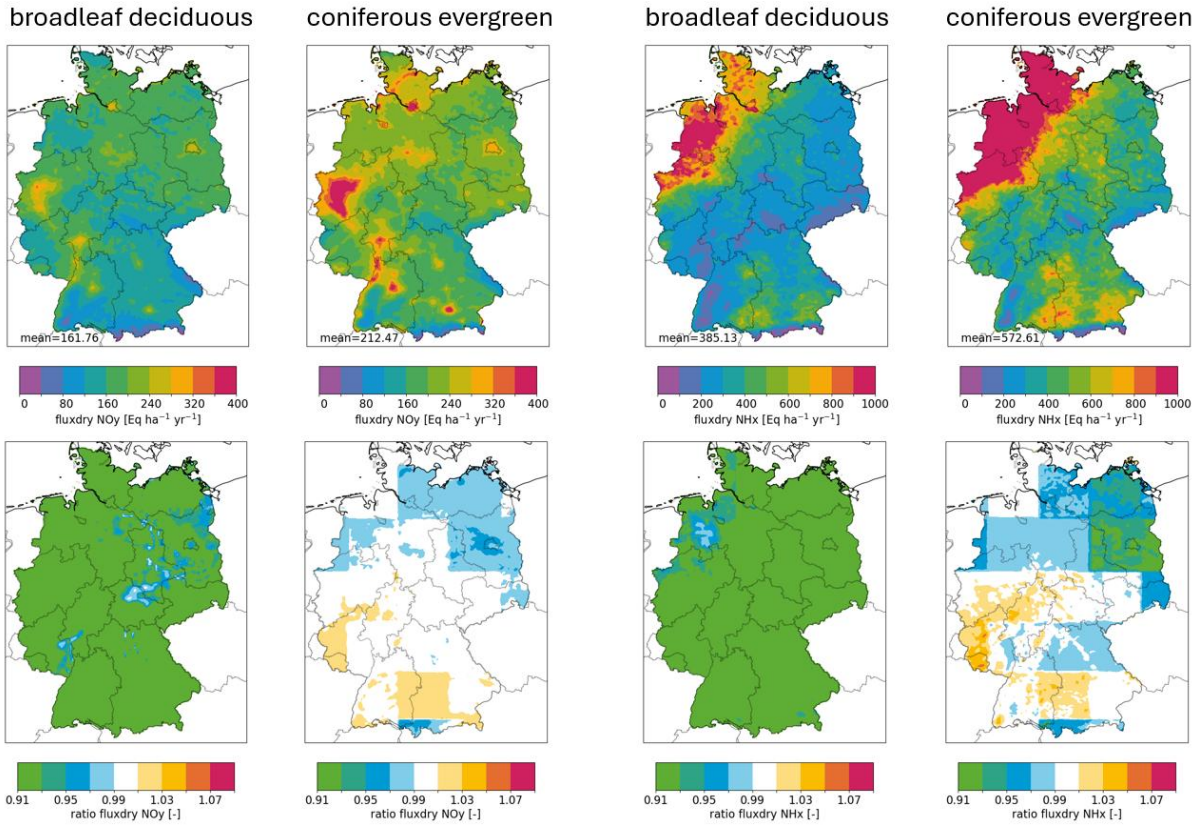

Figure 14: The NO_y and NH_x dry deposition flux for the broadleaf deciduous and coniferous evergreen forest land use class (columns). (top) the simulation result using rescaled satellite-derived LAI_{LE}, (bottom) the ratio between the ref and test run.

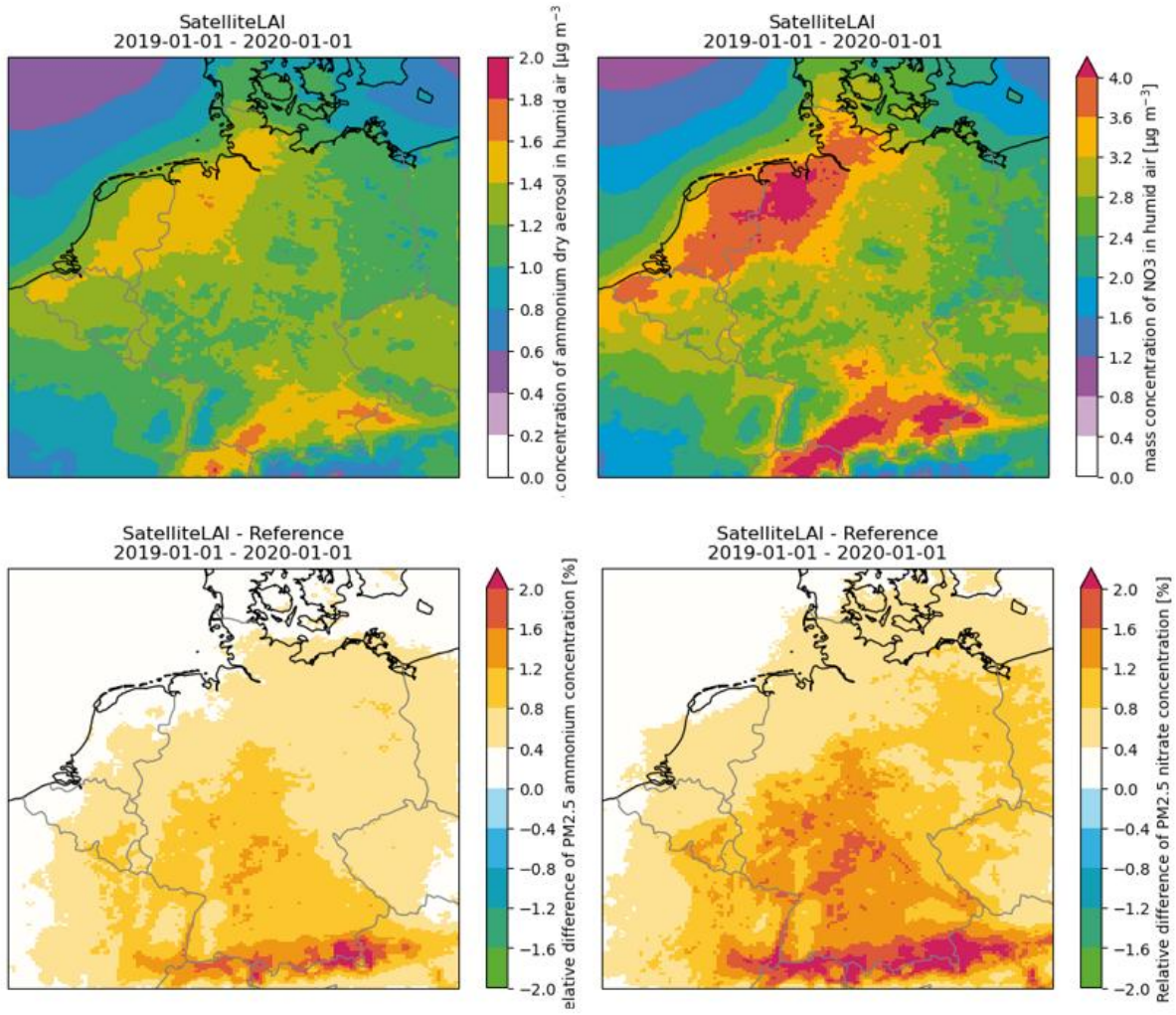

Figure 15: The maps and relative difference with respect to the reference run of aerosol (PM2.5) concentrations of nitrate and ammonium of the test run.

5.4 Conclusions

The MODIS LAI was masked with a broadleaf and coniferous tree mask. However, the resulting LAI showed anomalies. In the winter, the broadleaf tree LAI was not equal to zero and the coniferous (evergreen) forest LAI showed strong seasonality. Therefore, to retain the curvature of the satellite-derived LAI, but introduce the natural behavior of deciduous and evergreen forests, a rescaling was applied.

The resulting rescaled satellite-derived LAI_{LE} shows temporal characteristics such as the summer heat wave of 2003 leading to early decay of the LAI, and the warm spring in 2011 leading to early leaf growth. In addition, spatial variability throughout Germany was mainly observed in the maximum LAI of the coniferous trees and the start of the decay season of the broadleaf trees.

The sensitivity simulations performed with LOTOS-EUROS showed an overall decrease of deposition on N-compounds. In the northeast of Germany where predominantly coniferous trees are present, the reduced N-deposition is caused by the overall lower LAI_{LE} compared to the default LAI. In the southwest of Germany where there are predominantly broadleaf trees, the LAI_{LE} is lower in the spring compared to the default LAI which is the time period when the NH_3 concentration peaks due to manure application on arable land. Therefore, the NH_x dry

deposition flux is highly sensitive to the start of the growing season and we observe lowered NH_x deposition in the simulation.

A consequence of the decreased dry deposition of N-compounds, is the increased ammonium and nitrate PM2.5 concentration. The NH_3 and NO_2 that is not dry deposited, can now form aerosols. Thus, the regions with decreased gaseous dry deposition coincide with the regions of increased aerosol formation.

Lastly, to improve the LAI description, we suggested to improve the tree LAI description to prevent the checkerboard pattern of the blocks appears in the dry deposition flux ratio plot of NOy, which is probably also present for NH_x, but not visible due to the color scale (Figure 14). First, a mask is created by selecting only grid cells with >40% tree coverage based on a tree species map of Section 6.2.1.The tree species Abies spp., Alnus spp., Betula spp., Fagus spp., Larix spp., Pinus spp., Quercus spp., Picea spp., Pseudotsuga spp., Pinus Sylvestris, and Quercus Robur and Quercus Petraea obey this threshold. All other tree species can be treated as a default tree as already defined in LOTOS-EUROS.

To obtain a tree specific LAI, the satellite-derived LAI is cut in N x N number of blocks, and the LAI is averaged over those grid cells with >10 datapoints i.e. 10km^2. The number of blocks N is determined by visual inspection for each tree species such that the average of each block should represent its individual signals well and N is maximized to retrieve as much as spatial detail as possible. Naturally, not all blocks contain data as there might not be more than 10km^2 with >40% tree coverage. In order to obtain a LAI over the full domain for each tree species, the data is first interpolated in the longitudinal direction i.e. at constant latitude, as there is most correlation along this dimension. Then, the interpolation is performed along the latitudinal direction. In this way, the whole domain contains data for each tree species.

6 Tree species and height in deposition modelling

6.1 Introduction

Tree types and tree heights can influence nitrogen deposition by affecting how nitrogen is captured and retained in the ecosystems. Broadleaf and evergreen trees and taller forests generally capture more nitrogen, while coniferous and deciduous trees and shorter forests may capture less nitrogen but may process it more rapidly. It is important to understand these interactions for better estimating nitrogen deposition and the impacts of nitrogen pollution on ecosystems.

6.2 Method

6.2.1 Tree species

Tree species have a large impact on nitrogen deposition because they differ in the ability to capture, retain, and process atmospheric nitrogen caused by leaf characteristics, canopy structure, and physiological traits. Broadleaf trees with their high surface area-to-volume ratio (thin flat leaves) and evergreen trees with their all-year foliage, have generally higher potential for nitrogen interception per unit leaf mass and subsequently enhanced ability to capture nitrogen compounds. On the contrary, coniferous trees have thick or needle-like leaves and deciduous trees lose their leaves in winter, leading to less interception of atmospheric nitrogen. In addition, coniferous and evergreen forests, usually distributed densely, can intercept and capture more compared to open or less dense broadleaf and deciduous canopies.

Figure 16 demonstrates the bar chart showing estimated nitrogen deposition rates (in kg N ha^{-1} yr^{-1}) for different tree species (Norway Spruce (Picea abies), Scots Pine (Pinus sylvestris), Douglas Fir (Pseudotsuga menziesii), Oak (Quercus spp.), Beech (Fagus sylvatica), Birch (Betula spp.) and Eucalyptus spp.). These values are generalized averages based on forest canopy characteristics and literature data. One can see that the nitrogen deposition rate varies dramatically among tree species. The rate of birch (a broadleaf deciduous tree) is almost one third of that of Norway Spruce (a coniferous evergreen tree), which indicates that even though Norway Spruce has much thinner and narrower leaves, the fact that the leaves stay on all year round leads to a generally more deposition.

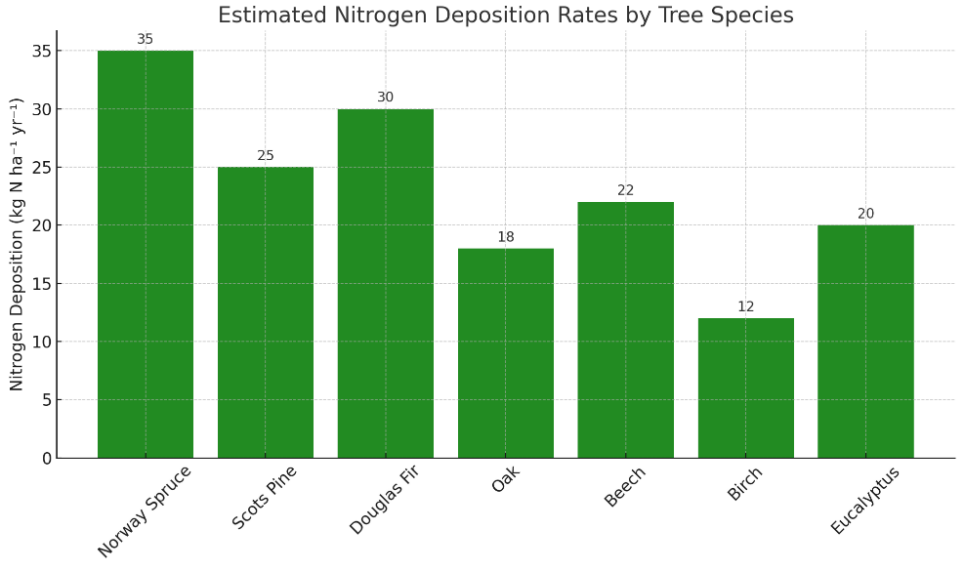

Figure 16: Estimated nitrogen deposition rate by different tree species based on literature study.

There are several datasets available on the distribution of tree species at the European or national scales. Brus et al. (2012) released a set of 1x1 km tree species maps showing the distribution of 20 tree species over Europe through statistical mapping (shown in Figure 17). It is apparent that Pinus sylvestris (coniferous evergreen) and Picea spp (coniferous evergreen) dominate in Northern and Southern Germany, respectively. While in Central Germany, there is a mixture of additional various tree species like Fagus spp (broadleaf deciduous), Populus spp (broadleaf deciduous), Quercus robur and Quercus petraea (broadleaf deciduous).

At the national level for example Germany, Blickensdörfer et al. (2024) used satellite data to derive the full-coverage, higher-resolution dominant tree species map. By using Sentinel-1/2 time series, the dominant tree species were classified by a machine-learning approach using their species-dependent spectral–phenological features. The mapping of the dominant tree species focused on the seven economically most important tree species in Germany. We combined the EU and German maps and used a translate table (shown in Table 6) to uniform the tree species from the two datasets. In total, 24 tree species are taken into account and are implemented into the three-tiered approach. The translated tree species map from Blickensdörfer et al. (2024) is demonstrated in Figure 18. The data has much better detail thanks to the high resolution of the Sentinel-1/2 observations. The map follows the similar pattern as shown in Figure 17, namely Pinus (coniferous evergreen) and Picea (coniferous evergreen) dominate in Northern and Southern Germany, respectively. Even though, Pinus and Picea are the most important tree species, area fraction maps of all tree species are created and fed into LOTOS-EUROS as input, given the complexity of the forest compositions. Besides, tree species vary in height, leaf property and growing season, etc., which is impactful in the deposition modeling scheme.

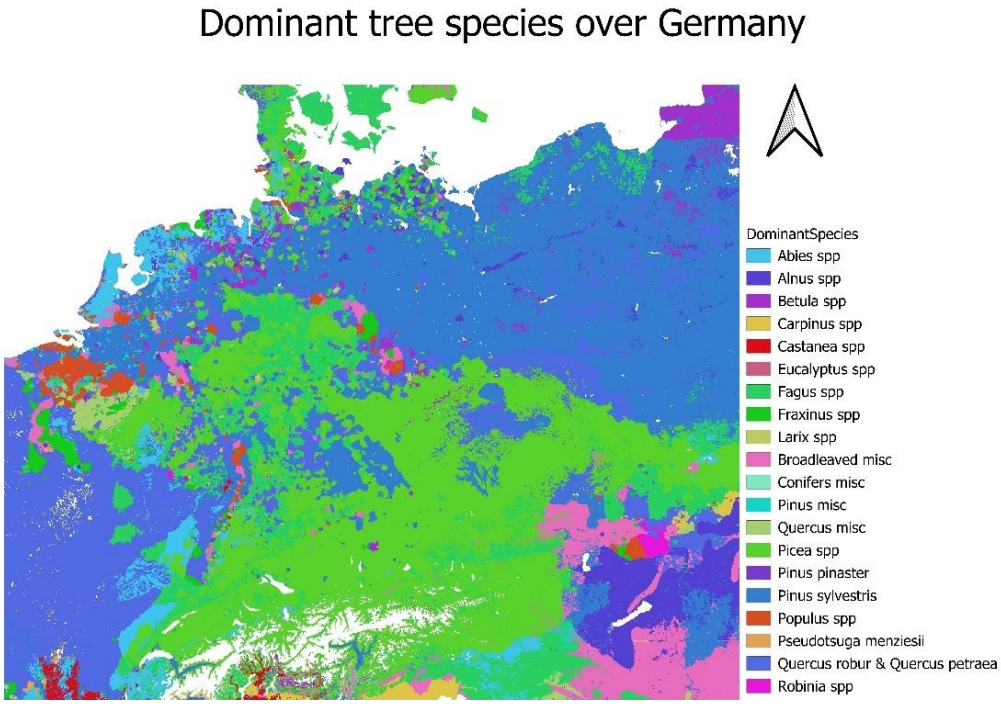

Figure 17: Dominant tree species over Germany using statistical mapping Brus et al. (2012).

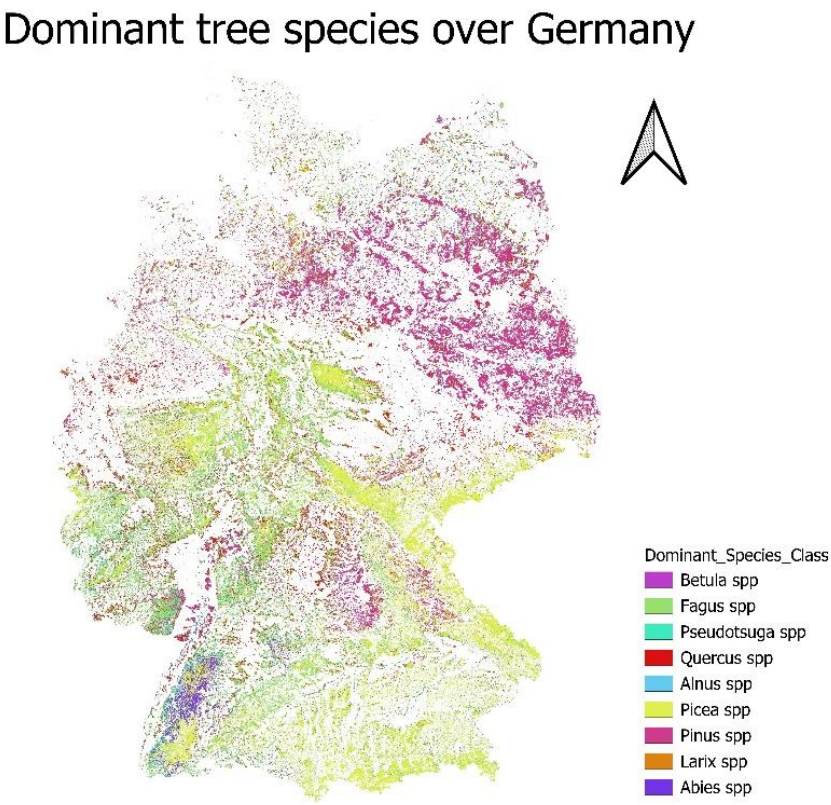

Figure 18: Dominant tree species over Germany using Sentinel-2 time series Blickensdörfer et al. (2024).

Table 6: Tree type classification after combining the EU and German scale tree species data.

Forest type code	Tree type code	Leaf Type	Leaf Change	Family	Tree Species Name	EU Species	DE Species
Fce	Abs	coniferous	evergreen	Pinaceae	Abies spp.	Abies Spp.	Fir
Fbd	Aln	broadleaf	deciduous	Betulaceae	Alnus spp.	Alnus Spp.	Alder
Fbd	Btl	broadleaf	deciduous	Betulaceae	Betula spp.	Betula Spp.	Birch
Fbd	Cpn	broadleaf	deciduous	Betulaceae	Carpinus spp.	Carpinus Spp.	
Fbd	Ctn	broadleaf	deciduous	Fagaceae	Castanea spp.	Castanea Spp.	
Fbe	Ect	broadleaf	evergreen	Myrtaceae	Eucalyptus spp.	Eucalyptus Spp.	
Fbd	Fgs	broadleaf	deciduous	Fagaceae	Fagus spp.	Fagus Spp.	Beech

Forest type code	Tree type code	Leaf Type	Leaf Change	Family	Tree Species Name	EU Species	DE Species
Fbd	Fxn	broadleaf	deciduous	Oleaceae	Fraxinus spp.	Fraxinus Spp.	
Fcd	Lrx	coniferous	deciduous	Pinaceae	Larix spp.	Larix Spp.	Larch
Fce	Pns	coniferous	evergreen	Pinaceae	Pinus spp.	Pines Misc.	Pine
Fbd	Qcs	broadleaf	deciduous	Fagaceae	Quercus spp.	Quercus Misc.	Oak
Fce	Pic	coniferous	evergreen	Pinaceae	Picea spp.	Picea Spp.	Spruce
Fce	Pnt	coniferous	evergreen	Pinaceae	Pinus pinaster	Pinus Pinaster	
Fce	Svt	coniferous	evergreen	Pinaceae	Pinus sylvestris	Pinus Sylvestris	
Fbd	Ppl	broadleaf	deciduous	Salicaceae	Populus spp.	Populus Spp.	
Fce	Pdg	coniferous	evergreen	Pinaceae	Pseudotsuga spp.	Pseudotsuga Menziesii	Douglas fir
Fbd	Grp	broadleaf	deciduous	Fagaceae	Quercus robur and Quercus petraea	Quercus Robur Petraea	
Fbd	Rbn	broadleaf	deciduous	Fagaceae	Robinia spp.	Robinia Spp.	
Fbd	Hls	broadleaf	deciduous		Other broadleaved deciduous with high life span		Other deciduous with high life span
Fbd	Lls	broadleaf	deciduous		Other broadleaved deciduous with low life span		Other deciduous with low life span
Fbd	Def	broadleaf	deciduous		Other broadleaved deciduous (Default)	Broadleaves	
Fbe	Def	broadleaf	evergreen		Other broadleaved		

Forest type code	Tree type code	Leaf Type	Leaf Change	Family	Tree Species Name	EU Species	DE Species
					evergreen (Default)		
Fcd	Def	coniferous	deciduous		Other conifers deciduous (Default)		
Fce	Def	coniferous	evergreen		Other conifers evergreen (Default)	Conifers	

6.2.2 Tree height

Tree height influences the vertical distribution of nitrogen deposition and the efficiency of nitrogen capture. Taller trees have larger canopies, allowing them to capture more nitrogen. Forests with a multi-layered canopy can intercept nitrogen at multiple heights, increasing overall nitrogen deposition. Tree height enters the deposition calculation as surface roughness. As mentioned in Section 4.2.1.1, roughness length defines the aerodynamic resistance and applies to the dry deposition of all species. Effectively, the higher the vegetation heights, the more the dry deposition of all species including gaseous species and aerosols.

Turubanova et al. (2023) obtained an annual tree canopy height dataset in Europe from 2001 to 2021 at a spatial resolution of around 30m using the Landsat archive and calibration data from Airborne Laser Scanning (ALS) and spaceborne Global Ecosystem Dynamics Investigation (GEDI) lidars. Annual tree canopy height was modeled using regression tree ensembles and integrated with annual tree canopy removal maps to produce harmonized tree height map time series. The tree height dataset has very high spatial resolution. On one hand, it offers extreme details on the forest extent, height distribution and yearly change; on the other hand, it increases the required processing power for data reading. Moreover, the spatial resolution of LOTOS-EUROS simulations is coarser, which means that the tree height data will have to be resampled to the model resolution before going into deposition calculations. As a result, the tree height data was resampled to the model run domain and resolution using a pre-processor. To account for the inconsistency between the tree species and tree height maps caused by difference data sources (e.g. there is no height information where trees exist), the median height of all trees in the area of interest (14m) is set to be the default value to replace the empty grid cells in the resampled tree height data.

The resampled tree height over Germany in 2019 is demonstrated in Figure 19 (left). It has to be noted that for areas where forests do not exist, a default value of 14 meters is used after calculating the medium tree height in the region. The relative difference between the updated tree height and the previously used default value (20 meters) is shown in Figure 19 (right). Combined with tree species map, there are following findings:

- In northern Germany along the border, where there are mixed tree species of Betula spp, Quercus robur & Quercus petraea, Abies spp, Populus spp, Alnus spp and Picea spp, tree height is as low as 4 – 8 meters, which is significantly lower than 20 meters (more than 50%).

- In northern Germany away from the border, where Pinus dominates, tree height is only little lower (less than 10%) than the default 20 meters.
- There is large decrease (between 30% and 50%) in tree height where Quercus robur & Quercus petraea dominate.
- In the majority of the forest area in Central and Southern Germany, tree height is 10% – 20% taller than 20 meters.

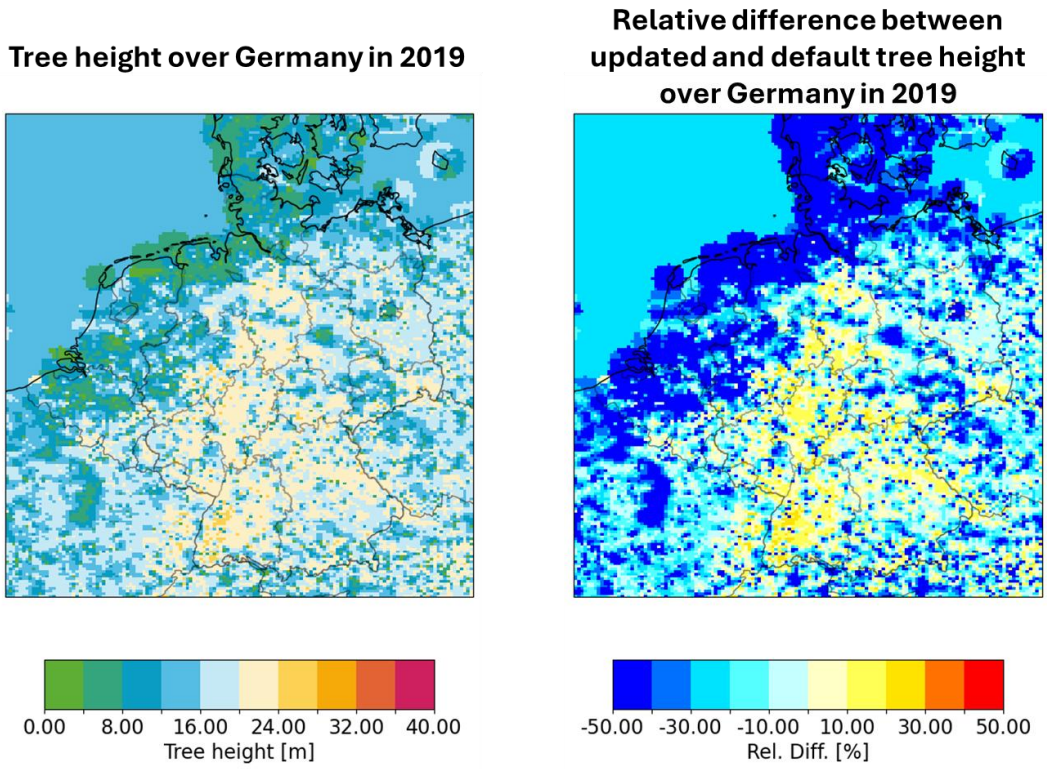

Figure 19: The tree height map (left) derived using Landsat archive (Turubanova et al., 2023) and relative difference (right) compared to the default value 20 meters over Germany in 2019.

6.3 Results

6.3.1 Wet deposition

The modelled wet deposition maps from the reference and updated simulations are illustrated in Figure 20. It can be seen that wet deposition barely had any changes, in terms of both the spatial distribution and mean value. This is also validated in Figure 21, which shows the comparisons of observed and modelled NH_4^{+1} and NO_3^{-1} wet depositions at German stations. The scatter plots are almost identical from the reference to the updated scenario.

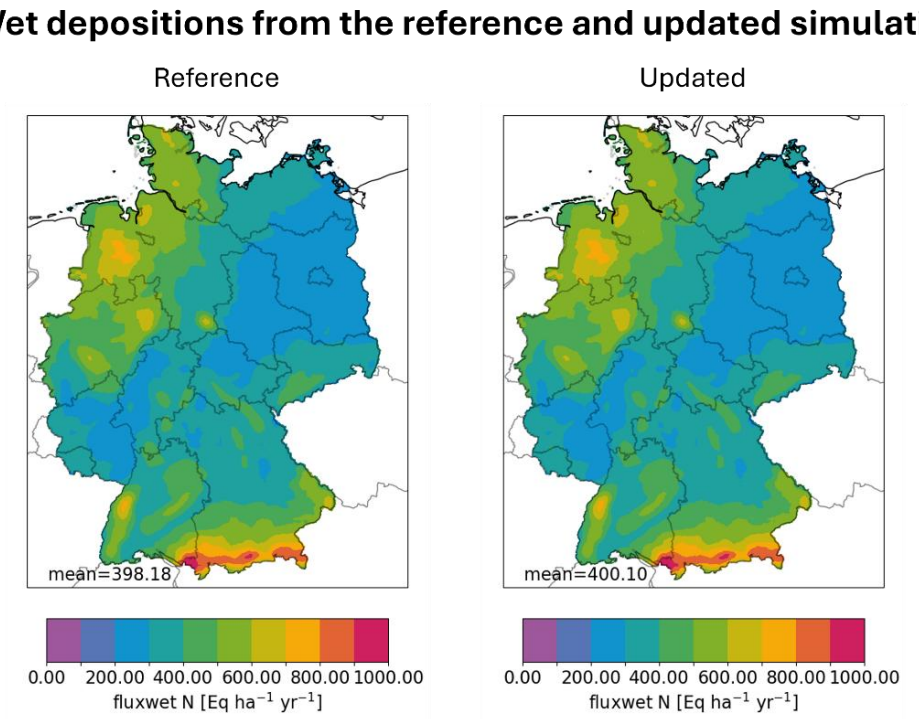

Figure 20: Modelled wet deposition from the reference (left) and updated (right) simulations.

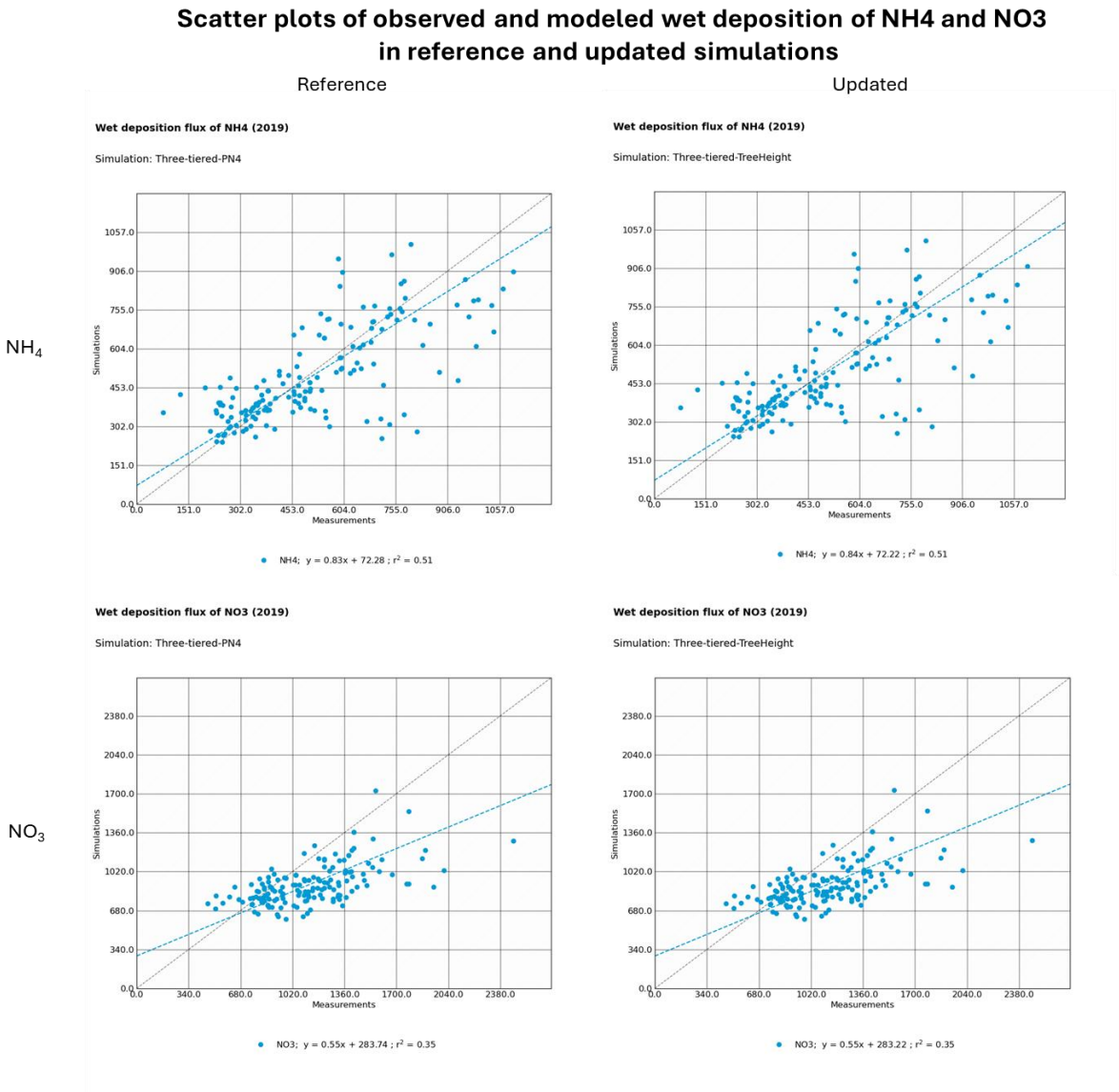

Figure 21: Comparisons of observed and modelled wet deposition of NH4 (upper panel) and NO3 (lower panel) in reference (left panel) and updated (right panel) simulations.

6.3.2 Dry deposition

The N dry depositions from the reference and updated simulations and their ratios on coniferous and broadleaf trees are demonstrated in Figure 22. By looking at the ratio between the reference and updated scenarios, the update in tree height leads to very similar change in the spatial distribution in dry deposition. One can notice the lower deposition in the north along the border, which is about 10% less than the modeled dry deposition in the reference simulation. The same pattern is found where Quercus robur & Quercus petraea dominate. The changes in these areas are more drastic because the three height decreases are also more prominent (more than 30%). Due to the small tree height difference in Pinus-dominated northern forests, the change in dry deposition is not very obvious. In Picea-dominated central and southern forests, the increase in tree height leads to 3% - 5% increase in dry deposition.

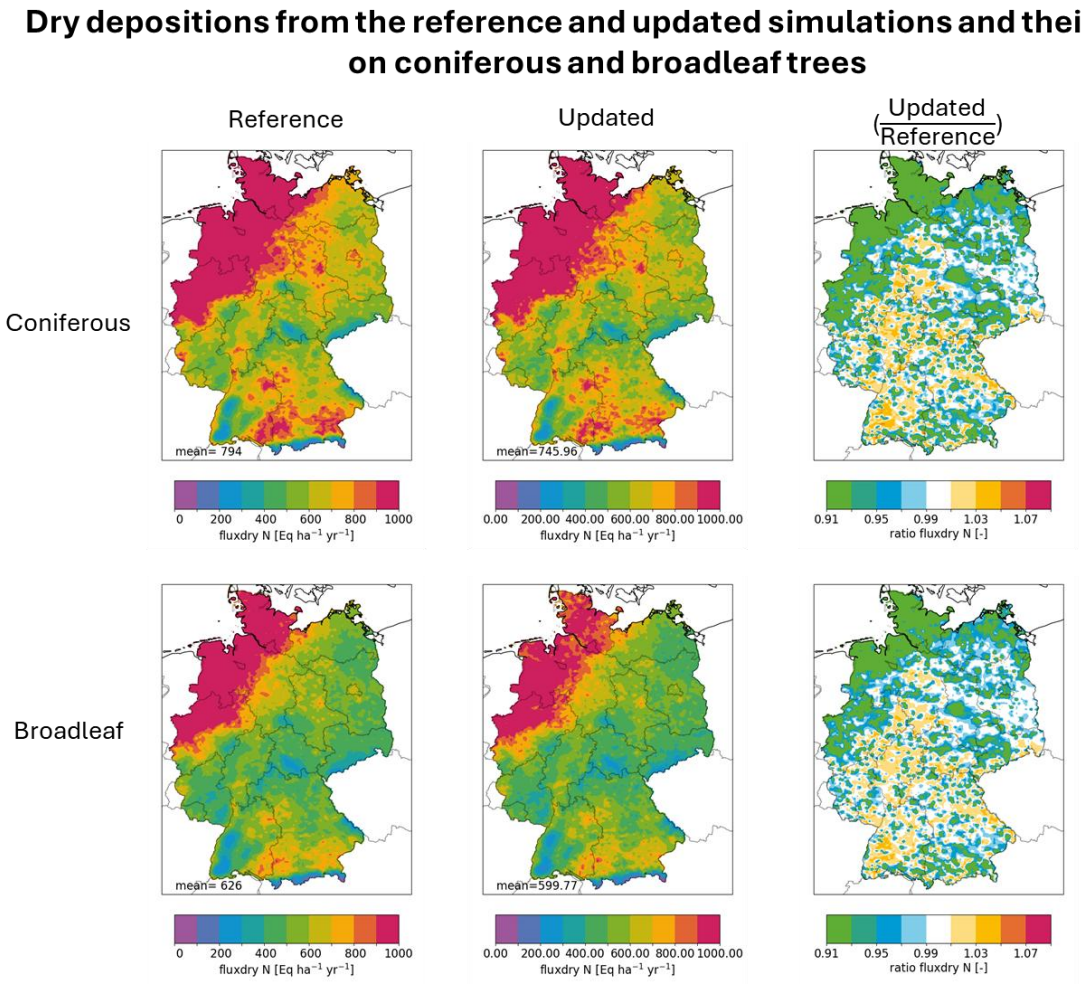

Figure 22: Dry depositions of N from the reference and updated simulations and their ratios on coniferous and broadleaf trees.

6.4 Conclusions

The updates on tree species and height have a significant impact on the spatial distribution of dry deposition of nitrogen but barely changes the wet deposition. There is more deposition in the central and southern Picea-dominated forest areas; whereas there are less where Quercus robur & Quercus petraea dominate and in the northern forests along the border. The results have shown the uncertainties and bias in the previous method where one default value of 20m for tree height was used. The update is especially important when it comes to policymaking in environmental protection because areas exceeding the critical loads might be ignored because inaccurate allocation of N deposition to the forests.

7 Overall conclusions

This study presents the development and evaluation of an extended dry deposition scheme by the integration a Three-Tiered Land Use Approach within the LOTOS-EUROS model. The Tree-Tiered Land Use Approach allows for differentiating vegetation-specific parameters, such as the leaf area index (LAI), maximal stomatal conductance, and growth season dynamics to specific (local) vegetations. Moreover, it makes it possible to differentiate between different vegetation types, e.g. crops, trees, or bushes, with different characteristics that were previously grouped in a single (land use) category.

In this work by leveraging this new approach, we detailed the vegetation-specific dry deposition parameters on forests, arable land and seminatural land. On forests, we updated the tree height and the LAI growing season based on satellite observations and differentiating various tree species. On arable land and semi-natural land, we updated the optimal, minimal, and maximal temperatures for stomatal opening, the minimum and maximum vapor pressure deficit, maximum leaf stomatal conductance, the vegetation height and the LAI growing season. With that, we significantly improved the model's ability to represent the spatial and temporal variability of nitrogen compound deposition.

The results show that the NO_y dry deposition patterns are related to the changes in vegetation parameters over the whole year. For example, the increased height and LAI_{max} of maize show an increased NOy dry deposition throughout Germany. Furthermore, incorporating tree species and height data revealed significant spatial shifts in dry deposition patterns, underscoring the limitations of previous uniform assumptions and the importance of species-specific modeling.

On the contrary for the NH_x dry-deposition, the timing of vegetation growth is critical, especially in the spring, when ammonia concentrations peak due to manure application. This seasonal sensitivity is seen for example on maize which shows less NH_x dry deposition due to its delayed LAI growth. Naturally, these updates also influence aerosol formation. Only in regions where both NH_x and NO_y dry deposition was decreased, increased concentrations of ammonium and nitrate PM2.5 were observed. This underscores the importance of detailing the dry deposition of the gaseous species and its relationship on the formation of particulate pollutants.

The next steps in Task 6.3 of the CAMAERA project will focus on integrating and testing the Three-Tiered Land Use Approach dry deposition scheme in the IFS model. Applying the approach in a different model will help to assess its broader applicability and indirectly supports its validation. Additionally, a comprehensive comparison of modeled and observed aerosol concentrations would be valuable for identifying potential shortcomings in the current representation of aerosol deposition. The Three-Tiered Land Use Approach's flexibility offers a useful basis for implementing and testing such targeted improvements.

8 References

Beck, H. E., Zimmermann, N. E., McVicar, T. R., Vergopolan, N., Berg, A., and Wood, E. F.: Present and future Köppen-Geiger climate classification maps at 1-km resolution, Sci. Data, 5, 180214, https://doi.org/10.1038/sdata.2018.214, 2018.

Op de Beeck, M., De Bock, M., Vandermeiren, K., de Temmerman, L., and Ceulemans, R.: A comparison of two stomatal conductance models for ozone flux modelling using data from two Brassica species, Environ. Pollut., 158, 3251–3260, https://doi.org/10.1016/j.envpol.2010.07.026, 2010.

Blickensdörfer, L., Oehmichen, K., Pflugmacher, D., Kleinschmit, B., and Hostert, P.: National tree species mapping using Sentinel-1/2 time series and German National Forest Inventory data, Remote Sens. Environ., 304, 114069, https://doi.org/https://doi.org/10.1016/j.rse.2024.114069, 2024.

Brus, D. J., Hengeveld, G. M., Walvoort, D. J. J., Goedhart, P. W., Heidema, A. H., Nabuurs, G. J., and Gunia, K.: Statistical mapping of tree species over Europe, Eur. J. For. Res., 131, 145–157, https://doi.org/10.1007/s10342-011-0513-5, 2012.

DWD Climate Data Center: Phenological observations of crops from sowing to harvest (annual reporters, recent), 2024.

CORINE Land Cover 2018 (raster 100 m), Europe, 6-yearly - version 2020_20u1, May 2020:

Joint Research Centre Data Catalogue - LUCAS Copernicus 2018 - European Commission: http://data.europa.eu/89h/cfe66a0c-bdee-4074-96e1-a2f7030b9515, last access: 21 May 2025.

Land Cover 2015 (raster 100 m), global, yearly – version 3 — Copernicus Land Monitoring Service: https://land.copernicus.eu/en/products/global-dynamic-land-cover/copernicus-global-land-service-land-cover-100m-collection-3-epoch-2015-globe, last access: 21 May 2025.

Forest Type 2018 (raster 10 m, 100 m), Europe, 3-yearly — Copernicus Land Monitoring Service: https://land.copernicus.eu/en/products/high-resolution-layer-forests-and-tree-cover/forest-type-2018-raster-10-m-100-m-europe-3-yearly, last access: 21 May 2025.

Ghassemi-Golezani, K., Rajabi, M., and Farzi-Aminabad, R.: Improving physiological performance and productivity of oilseed rape under drought stress by foliar application of Zn and Mg nanoparticles, J. Plant Physiol. Breed., 2023, 217–229, https://doi.org/10.22034/JPPB.2023.56387.1304, 2024.

Guevara, M., Colette, A., Guion, A., Petiot, V., Adani, M., Arteta, J., Benedictow, A., Bergström, R., Bolignano, A., Camps, P., Carvalho, A. C., Christensen, J. H., Couvidat, F., D'Elia, I., van der Gon, H., Descombes, G., Douros, J., Fagerli, H., Fatahi, Y., Friese, E., Frohn, L., Gauss, M., Geels, C., Hänninen, R., Hansen, K., Jorba, O., Kaminski, J. W., Kouznetsov, R., Kranenburg, R., Kuenen, J., Lannuque, V., Meleux, F., Ny\'\iri, A., Palamarchuk, Y., Pérez Garc\'\ia-Pando, C., Robertson, L., Russo, F., Segers, A., Sofiev, M., Struzewska, J., Timmermans, R., Uppstu, A., Valdebenito, A., and Ye, Z.: Technical note: Sensitivity of the CAMS regional air quality modelling system to anthropogenic emission temporal variability, EGUsphere, 2025, 1–47, https://doi.org/10.5194/egusphere-2025-1287, 2025.

Jay, S., Maupas, F., Bendoula, R., and Gorretta, N.: Retrieving LAI, chlorophyll and nitrogen contents in sugar beet crops from multi-angular optical remote sensing: Comparison of vegetation indices and PROSAIL inversion for field phenotyping, F. Crop. Res., 210, 33–46, https://doi.org/10.1016/j.fcr.2017.05.005, 2017.

Kaiser, J. W., Heil, A., Andreae, M. O., Benedetti, A., Chubarova, N., Jones, L., Morcrette, J.-J., Razinger, M., Schultz, M. G., Suttie, M., and van der Werf, G. R.: Biomass burning

emissions estimated with a global fire assimilation system based on observed fire radiative power, Biogeosciences, 9, 527–554, https://doi.org/10.5194/bg-9-527-2012, 2012.

Kuenen, J., Dellaert, S., Visschedijk, A., Jalkanen, J.-P., Super, I., & Denier van der Gon, H. (2022). CAMS-REG-v4: a state-of-the-art high-resolution. *Earth Syst. Sci. Data, 14*, 491–515.

Manders, A., Segers, A., Kranenburg, R., Jonas, H., Hohenberger, T., and Geers, L.: LOTOS-EUROS v3.0.000 Reference Guide, 2025.

Melkonian, J.: Chilling responses of maize (Zea mays L.) seedlings: root hydraulic conductance, abscisic acid, and stomatal conductance, J. Exp. Bot., 55, 1751–1760, https://doi.org/10.1093/jxb/erh215, 2004.

Mills, G., Pleijel, H., Büker, P., Braun, S., Emberson, L., Harmens, H., Hayes, F., Simpson, D., Grünhage, L., and Karlsson, P. E.: Chapter 3: Mapping critical levels for vegetation, Man. Methodol. Criteria Model. Mapp. Crit. Loads Levels Air Pollut. Eff. Risks Trends, 2010.

Raboanatahiry, N., Li, H., Yu, L., and Li, M.: Rapeseed (Brassica napus): Processing, Utilization, and Genetic Improvement, Agronomy, 11, 1776, https://doi.org/10.3390/agronomy11091776, 2021.

Segers, A., Manders, A., Kranenburg, R., Jonas, H., Hohenberger, T., and Geers, L.: LOTOS-EUROS User Guide v3.0.000, 2025.

Sinsawat, V., Leipner, J., Stamp, P., and Fracheboud, Y.: Effect of heat stress on the photosynthetic apparatus in maize (Zea mays L.) grown at control or high temperature, Environ. Exp. Bot., 52, 123–129, https://doi.org/10.1016/j.envexpbot.2004.01.010, 2004.

Sun, B., Wang, C., Yang, C., Xu, B., Zhou, G., Li, X., Xie, J., Xu, S., Liu, B., Xie, T., Kuai, J., and Zhang, J.: Retrieval of rapeseed leaf area index using the PROSAIL model with canopy coverage derived from UAV images as a correction parameter, Int. J. Appl. Earth Obs. Geoinf., 102, 102373, https://doi.org/10.1016/j.jag.2021.102373, 2021.

Taube, F., Vogeler, I., Kluß, C., Herrmann, A., Hasler, M., Rath, J., Loges, R., and Malisch, C. S.: Yield Progress in Forage Maize in NW Europe—Breeding Progress or Climate Change Effects?, Front. Plant Sci., 11, 1–16, https://doi.org/10.3389/fpls.2020.01214, 2020.

Turubanova, S., Potapov, P., Hansen, M. C., Li, X., Tyukavina, A., Pickens, A. H., Hernandez-Serna, A., Arranz, A. P., Guerra-Hernandez, J., Senf, C., Häme, T., Valbuena, R., Eklundh, L., Brovkina, O., Navrátilová, B., Novotný, J., Harris, N., and Stolle, F.: Tree canopy extent and height change in Europe, 2001–2021, quantified using Landsat data archive, Remote Sens. Environ., 298, 113797, https://doi.org/https://doi.org/10.1016/j.rse.2023.113797, 2023.

Umweltbundesamt: German Informative Inventory Report 2022 (IIR 2022)., 2022.

Verger, A., Sánchez-Zapero, J., Weiss, M., Descals, A., Camacho, F., Lacaze, R., and Baret, F.: GEOV2: Improved smoothed and gap filled time series of LAI, FAPAR and FCover 1 km Copernicus Global Land products, Int. J. Appl. Earth Obs. Geoinf., 123, 103479, https://doi.org/https://doi.org/10.1016/j.jag.2023.103479, 2023.

van Zanten, M. C. van, Sauter, F. J., Kruit, R. J. W., J.A. van Jaarsveld, P., and Pul, W. A. J. van: Description of the DEPAC module, 1–76, 2010.

Zhang, L., Gong, S., Padro, J., and Barrie, L.: A size-segregated particle dry deposition scheme for an atmospheric aerosol module, Atmos. Environ., 35, 549–560, https://doi.org/https://doi.org/10.1016/S1352-2310(00)00326-5, 2001.

Zhang, L., Brook, J. R., and Vet, R.: A revised parameterization for gaseous dry deposition in air-quality models, Atmos. Chem. Phys., 3, 2067–2082, https://doi.org/10.5194/acp-3-2067-2003, 2003.

Document History

Version	Author(s)	Date	Changes
1.0	H.J. Jonas, X. Ge, L. Geers, R. Kranenburg, C. Halevy	30 May 2025	Initial version
1.1	H.J. Jonas, X. Ge, L. Geers, R. Kranenburg, C. Halevy	26 June 2025	Final version

Internal Review History

Internal Reviewers	Date	Comments
Vincent Huijnen (KNMI)	12 June 2025	Minor comments